Gravitational waves, bubble profile, and baryon asymmetry in the complex 2HDM

Dorival Gonçalves[1,*], Ajay Kaladharan[1,†] and Yongcheng Wu[2,1,‡]

[1]*Department of Physics, Oklahoma State University, Stillwater, Oklahoma 74078, USA*
[2]*Department of Physics and Institute of Theoretical Physics, Nanjing Normal University, Nanjing 210023, China*

This study explores the generation of the observed baryon asymmetry of the Universe within the complex two-Higgs doublet model (C2HDM) while considering theoretical and current experimental constraints. In our investigation, we analyze critical elements of the Higgs potential to understand the phase-transition pattern. Specifically, we examine the formation of the barrier and the uplifting of the true vacuum state, which play crucial roles in facilitating a strong first-order phase transition. Furthermore, we explore the potential gravitational wave signals associated with this phase transition pattern and investigate the parameter space points that can be probed with LISA. Finally, we compare the impact of different approaches to describing the bubble profile on the calculation of the baryon asymmetry. We contrast the typically used kink profile approximation against the explicit solution of the tunneling profile. We find that a non-negligible range of the C2HDM parameter space results in significant discrepancies in the baryon asymmetry estimation between these two approaches. Through an examination of the parameter space, we identify a benchmark point that satisfies the observed baryon asymmetry.

I. INTRODUCTION

Understanding the origin of the matter-antimatter asymmetry of the Universe, known as the baryon asymmetry of the Universe (BAU), is a fundamental question in particle physics and cosmology. The asymmetry between baryons and antibaryons in the early Universe can be quantitatively evidenced through the baryon-to-entropy ratio measurement $n_B/s \simeq 8.6 \times 10^{-11}$ [1], exceeding the expected value for a symmetric scenario by several orders of magnitude. As a consequence, the majority of antibaryons underwent annihilation during the thermal history, leaving behind a significant density of baryons in the present Universe. The essential ingredients required for generating this baryon asymmetry are theoretically well-understood and encapsulated by the three Sakharov conditions [2]. These conditions demand the violation of baryon number, the presence of C and CP violation, and a departure from thermal equilibrium. While the Standard Model (SM)

satisfies the requirements for baryon number violation and C violation, it falls short in providing a sufficiently robust source of CP violation. Additionally, the observed Higgs mass of $m_h = 125$ GeV precludes the necessary out-of-equilibrium conditions through a strong first-order phase transition [3,4]. Thus, the quest for baryogenesis requires physics beyond the SM [5–8].

Among possible extensions, the complex two-Higgs doublet model (C2HDM) can potentially provide both of the missing ingredients; strong first-order electroweak phase transition and additional sources of CP violation [9–11]. In this work, we explore the phase transition pattern and the feasibility of generating the observed baryon asymmetry within the context of the C2HDM. Central to our investigation is the shape of the Higgs potential, which plays a crucial role in determining the nature of the phase transition. We focus on the formation of the barrier and the upliftment of the true vacuum state, as these factors are instrumental in driving the phase transition from a smooth crossover to a strong first-order transition. Our analysis builds upon previous studies for other new physics extensions [12–15], where it was observed that the intensity of the phase transition is closely linked to the elevation of the true vacuum relative to the symmetric one at zero temperature. The prevalence of one-loop effects over thermal corrections, particularly when $\xi_c > 1$, enhances the strength of the phase transition [15]. However, it should be noted that if the one-loop correction is too large, the Universe may become

[*]dorival@okstate.edu
[†]kaladharan.ajay@okstate.edu
[‡]ycwu@njnu.edu.cn

trapped in the electroweak symmetric vacuum, resulting in an incomplete phase transition [15,16]. Consequently, as we will show, a significant portion of parameter points with large ξ_c values become unphysical in this scenario.

The first-order phase transition in the early Universe can generate stochastic gravitational waves (GW) whose characteristic peak frequency is associated with the phase transition temperature. After redshifting to the present time, the GW spectrum would have a peak frequency at the mHz range for the phase transition at the electroweak scale [17,18]. This presents an exciting prospect to probe electroweak phase transition (EWPT) at LISA [19], designed to be sensitive to mHz frequency signals. Hence, we also investigate the parameter space points in C2HDM that can be probed using LISA.

Through an extensive exploration of the parameter space, we note that the C2HDM can describe the observed baryon asymmetry, although only for a limited set of parameter space points. In this regard, we compare two different approaches to describe the bubble profile, a key ingredient in the BAU estimation. The commonly adopted kink-profile parametrization [20–24] and the explicit solution for the tunneling equation are examined to assess their impact on the resulting baryon asymmetry. Our analysis reveals relevant deviations between the BAU calculation between these two approaches. While the majority of parameter space points yield similar results using both methods, a notable fraction exhibits significant differences, sometimes varying by several orders of magnitude. To understand these discrepancies, we scrutinize the behavior of the source term in front of the bubble wall, which sheds light on the distinct asymmetry values obtained from the two profile assumptions.

The paper is organized as follows. In Sec. II, we provide a brief overview of the complex two-Higgs double model. Section III discusses the one-loop finite temperature effective potential. It is followed by a discussion on electroweak phase transition and GW signals in Sec. IV. In Sec. V, we study how the shape of the Higgs potential will affect the EWPT, focusing on the barrier formation and the vacuum upliftment. In Sec. VI, we present the details for the baryon asymmetry calculation. The results of the BAU are presented in Sec. VII, where we also contrast the results depending on the bubble profile estimation. Finally, we summarize in Sec. VIII. Details of the parameterization for the C2HDM scan are presented in Appendix A.

II. COMPLEX TWO-HIGGS DOUBLET MODEL

The two-Higgs doublet model (2HDM) lays out a compelling extension of the SM in line with current experimental constraints [25]. This work considers CP-violating 2HDM with a softly broken $\mathbb{Z}_2$ symmetry. Within this framework, the tree-level potential is given by

$$
\begin{aligned}
V_0(\Phi_1, \Phi_2) = {} & m_{11}^2 \Phi_1^\dagger \Phi_1 + m_{22}^2 \Phi_2^\dagger \Phi_2 - (m_{12}^2 \Phi_1^\dagger \Phi_2 + \text{H.c.}) \\
& + \frac{\lambda_1}{2}(\Phi_1^\dagger \Phi_1)^2 + \frac{\lambda_2}{2}(\Phi_2^\dagger \Phi_2)^2 \\
& + \lambda_3(\Phi_1^\dagger \Phi_1)(\Phi_2^\dagger \Phi_2) + \lambda_4(\Phi_1^\dagger \Phi_2)(\Phi_2^\dagger \Phi_1) \\
& + \left(\frac{\lambda_5}{2}(\Phi_1^\dagger \Phi_2)^2 + \text{H.c.}\right),
\end{aligned} \tag{1}
$$

where the mass term m_{12}^2 and quartic coupling λ_5 are complex and all other mass terms and quartic couplings are taken to be real. However, one of the phases in m_{12}^2 and λ_5 can be removed by a phase redefinition of Φ_2. In this work, we always keep m_{12}^2 real and λ_5 will be complex at zero temperature. Hence, overall in such setup, there is only one independent physical CP violation phase. To preclude dangerous tree-level flavor-changing neutral currents (FCNC) [26,27], we impose a $\mathbb{Z}_2$ symmetry softly broken by the m_{12}^2 term, under which $\Phi_1 \to \Phi_1$ and $\Phi_2 \to -\Phi_2$. Following electroweak symmetry breaking, the neutral components of Φ_1 and Φ_2 develop nonzero vacuum expectation values (VEVs).

Expanding around the VEVs ω_i, the scalar doublets Φ_i can be written as

$$
\Phi_1 = \begin{pmatrix} H_1^+ \\ \frac{\omega_1 + H_1^0 + i A_1^0}{\sqrt{2}} \end{pmatrix} \quad \text{and} \quad \Phi_2 = e^{i\omega_\theta} \begin{pmatrix} H_2^+ + \frac{\omega_{CB}}{\sqrt{2}} \\ \frac{\omega_2 + H_2^0 + i A_2^0}{\sqrt{2}} \end{pmatrix}, \tag{2}
$$

where at zero temperature VEVs $v_i \equiv \omega_i|_{T=0}$, $i = 1,\ 2$ are linked to SM VEV by $v_1^2 + v_2^2 = v^2 \approx (246 \text{ GeV})^2$. Whereas an additional source of CP-violation should decrease at zero temperature $(\omega_\theta|_{T=0} \to 0)$ to comply with the stringent electric dipole moment (EDM) constraints [28], the dynamical generation of CP-violation at high temperatures offers a potential avenue for a CP-violating mechanism crucial to the success of electroweak baryogenesis. To account for a more comprehensive scenario, we also incorporate a possible charge-breaking VEV at high temperature, ω_{CB}. Since a nonzero charge-breaking VEV at zero temperature would lead to massive photons, we impose $v_{CB} = 0$.

The scalar sector in the CP-violating 2HDM has five physical mass eigenstates; three CP-mixed neutral scalars H_i and one charged scalar pair $H^\pm$. The correspondence between mass eigenstates and gauge eigenstates is established by the mixing angle β in CP-odd and charged sectors and another three angles α, α_b and α_c mixing the CP-odd and CP-even scalars,

$$
\begin{pmatrix} G^\pm \\ H^\pm \end{pmatrix} = \begin{pmatrix} c_\beta & s_\beta \\ -s_\beta & c_\beta \end{pmatrix} \begin{pmatrix} H_1^\pm \\ H_2^\pm \end{pmatrix}, \qquad \begin{pmatrix} G^0 \\ A \end{pmatrix} = \begin{pmatrix} c_\beta & s_\beta \\ -s_\beta & c_\beta \end{pmatrix} \begin{pmatrix} A_1^0 \\ A_2^0 \end{pmatrix}, \tag{3}
$$

$$
\begin{pmatrix} H_1 \\ H_2 \\ H_3 \end{pmatrix} = O \begin{pmatrix} H_1^0 \\ H_2^0 \\ A \end{pmatrix} = \begin{pmatrix} -s_\alpha c_{\alpha_b} & c_\alpha c_{\alpha_b} & s_{\alpha_b} \\ c_\alpha c_{\alpha_c} + s_\alpha s_{\alpha_b} s_{\alpha_c} & s_\alpha c_{\alpha_c} - c_\alpha s_{\alpha_b} s_{\alpha_c} & c_{\alpha_b} s_{\alpha_c} \\ -c_\alpha s_{\alpha_c} + s_\alpha s_{\alpha_b} c_{\alpha_c} & -s_\alpha s_{\alpha_c} - c_\alpha s_{\alpha_b} c_{\alpha_c} & c_{\alpha_b} c_{\alpha_c} \end{pmatrix} \begin{pmatrix} H_1^0 \\ H_2^0 \\ A \end{pmatrix}.
\tag{4}
$$

The mixing angle β is defined as $t_\beta \equiv \tan\beta = v_2/v_1$ ($\cos\beta \equiv c_\beta$ $\sin\beta \equiv s_\beta$). We also define $c_x \equiv \cos x$ and $s_x \equiv \sin x$.

At zero temperature, the physical parameters in the scalar sector include the VEVs ($v_1 = v c_\beta$, $v_2 = v s_\beta$, $\theta \equiv \langle \omega_\theta \rangle$), the masses of the scalar eigenstates (m_{H_i} and $m_{H^\pm}$), the mixing angles (α, α_b, and α_c), and m_{12}^2. Note that, as we mentioned earlier, there is only one physical CP-violation phase, i.e., only one of θ, α_b, and α_c is independent. In this work, we keep α_c as an independent input while calculating θ and α_b from other parameters. Hence, we choose the input parameters to be

$$
\begin{aligned}
v &= 246 \text{ GeV}, \quad t_\beta, c_{\beta-\alpha}, \alpha_c, \ m_{12}^2, \\
m_h &= 125 \text{ GeV}, \quad m_{H_\uparrow}, \ m_{H_\downarrow}, \ m_{H^\pm},
\end{aligned}
\tag{5}
$$

which match the nine real parameters in the potential Eq. (1). Here, $m_{H_\uparrow}$ and $m_{H_\downarrow}$ represent the masses of heavier and lighter beyond the Standard Model (BSM) neutral scalars, respectively. The detailed mapping between the parameters in Eq. (5) and those in Eq. (1) can be found in Appendix A. This parametrization for the CP-violating 2HDM is similar to the scan performed for CP-conserving 2HDM in our earlier works [15,29] in the sense that it provides scans over all physical BSM scalar masses ($m_{H_\uparrow}$, $m_{H_\downarrow}$, and $m_{H^\pm}$) and the CP-violating angle (α_c). The phase transition pattern in 2HDM, to a large extent, depends on the masses of additional scalars and corresponding mass splittings [15]. Hence, the numerical scan performed over three scalar masses is more suitable than one of the scalar masses written as a function of other scan variables.

Within the Yukawa sector, there are four distinct $\mathbb{Z}_2$ charge assignments that effectively preclude tree-level FCNC. In this study, we focus on two specific scenarios; Type-I and Type-II. In the Type-I scenario, all fermions exclusively couple with Φ_2, while in the Type-II scenario, only up quarks couple with Φ_2, with down quarks and charged leptons coupling with Φ_1. To thoroughly explore these possibilities, we conduct a random uniform scan, encompassing both Type-I and Type-II configurations over the parameter-space region,

$$
\tan\beta \in (0.8, 25), \qquad m_{12}^2 \in (10^{-3}, 5 \times 10^5) \text{ GeV}^2, \qquad m_{H_{\uparrow/\downarrow}} \in (30, 1500) \text{ GeV},
$$

$$
\alpha_c \in \left(-\frac{\pi}{2}, \frac{\pi}{2} \right), \qquad \cos(\beta - \alpha) \in (-0.3, 0.3), \qquad m_{H^\pm} \in (150, 1500) \text{ GeV}.
\tag{6}
$$

We perform the parameter-space scan by implementing the parametrization detailed in Appendix A in ScannerS [30,31]. Using ScannerS, we impose constraints from perturbative unitarity [32–34], boundedness from below [35], vacuum stability [36,37], electroweak precision, and flavor constraints. EDM constraints are also imposed using the stringent limits from the ACME Collaboration [28]. Furthermore, constraints from the 125 GeV Higgs-boson measurements and additional scalar searches are carried out using HiggsBounds and HiggsSignals [38–40].

III. ONE-LOOP FINITE TEMPERATURE EFFECTIVE POTENTIAL

We use loop-corrected finite temperature effective potential to determine the dynamics of electroweak symmetry breaking in the early Universe. Along with the tree-level potential V_0 from Eq. (1), we also include the Coleman-Weinberg potential V_{CW} and counterterms V_{CT} that encode one-loop corrections at zero temperature, and finite-temperature corrections V_T. The effective potential is given by

$$
V_{\text{eff}} = V_0 + V_{\text{CW}} + V_{\text{CT}} + V_T.
\tag{7}
$$

The Coleman-Weinberg potential in the Landau gauge can be written, using $\overline{\text{MS}}$ renormalization prescription as [41]

$$
V_{\text{CW}} = \sum_i \frac{n_i}{64\pi^2} m_i^4(\Phi_1, \Phi_2) \left[\log\left(\frac{m_i^2(\Phi_1, \Phi_2)}{\mu^2} \right) - c_i \right],
\tag{8}
$$

where the index i runs over all particles in the thermal bath with field-dependent mass $m_i(\Phi_1, \Phi_2)$, including Higgs bosons, massive gauge bosons, Goldstone bosons, longitudinal photon, and fermions. The parameter n_i represents the number of degrees of freedom for each particle, with $n_i > 0$ for bosons and $n_i < 0$ for fermions. In the $\overline{\text{MS}}$

renormalization procedure, the coefficient c_i takes the value of 5/6 for gauge bosons and 3/2 otherwise. Moreover, we set the renormalization scale μ to the zero-temperature VEV, $\mu = v(T = 0) \approx 246$ GeV.[1]

The one-loop effects of the Coleman-Weinberg potential result in shifts of the mixing angle and scalar masses from their tree-level values. To perform a consistent parameter scan, we adopt an on shell renormalization scheme, which enforces the parameters to match their tree-level values [24,44,45], by proper counterterms determined according to

$$\partial_{\phi_i}(V_{\text{CW}} + V_{\text{CT}})|_{\omega=\omega_{\text{tree}}} = 0, \tag{9}$$

$$\partial_{\phi_i}\partial_{\phi_j}(V_{\text{CW}} + V_{\text{CT}})|_{\omega=\omega_{\text{tree}}} = 0, \tag{10}$$

where ϕ_i $(i = 1, \ldots, 8)$ represents scalar components from the Φ_1 and Φ_2 doublets, ω denotes the ω_i values, and ω_{tree} characterizes the minimum of the tree-level potential for the fields in Φ_1 and Φ_2. The first and second derivatives of V_{CW} are consistently defined with an analytical expression in Ref. [44].[2] The first renormalization condition, given by Eq. (9), ensures that the minimum of the effective potential is not shifted from tree-level minimum, and the second condition, shown in Eq. (10), guarantees that mixing angles and scalar masses remain the same as their tree-level values.

The one-loop thermal correction V_T in Eq. (7) is given by [48]

$$V_T = \frac{T^4}{2\pi^2}\left[\sum_f n_f J_+\left(\frac{m_f^2}{T^2}\right) + \sum_{\mathcal{V}_T} n_{\mathcal{V}_T} J_-\left(\frac{m_{\mathcal{V}_T}^2}{T^2}\right)\right. \\ \left. + \sum_{\mathcal{V}_L} n_{\mathcal{V}_L} J_-\left(\frac{m_{\mathcal{V}_L}^2}{T^2}\right)\right] - \frac{T^4}{2\pi^2}\sum_{\mathcal{V}_L}\frac{\pi}{6}\left(\frac{\bar{m}_{\mathcal{V}_L}^3}{T^3} - \frac{m_{\mathcal{V}_L}^3}{T^3}\right), \tag{11}$$

where the sum extends over fermions f and bosons. The bosonic sector can be further divided into two categories; the transverse modes of gauge bosons, represented by $\mathcal{V}_T = W_T, Z_T$, and the longitudinal modes of gauge bosons and scalars, denoted by $\mathcal{V}_L = W_L, Z_L, \gamma_L, \Phi^0, \Phi^\pm$. The resummation of the $n = 0$ Matsubara modes of the longitudinal components $\mathcal{V}_L$ leads to thermal corrections in their masses [49,50]. The second line in Eq. (11) corresponds to the Daisy contributions, where $\bar{m}_{\mathcal{V}_L}$ represents the thermal

Debye mass calculated using the Arnold-Espinosa scheme [45,48]. The formulas for Debye masses are provided in Appendix C. Finally, the thermal functions for fermions (J_+) and bosons (J_-) are given by

$$J_\pm(x) = \mp \int_0^\infty dy\, y^2 \log\left(1 \pm e^{-\sqrt{y^2+x^2}}\right). \tag{12}$$

Whereas the effective potential in the electroweak phase transition is subject to theoretical uncertainties stemming from gauge parameter choices [42,51–57], Nielsen identities offer a way to construct gauge-independent probes [58]. These identities ensure that the gauge dependence cancels out at the extrema of the potential

$$\frac{\partial V_{\text{eff}}(\Phi_1, \Phi_2, \xi)}{\partial \xi} = -C_i(\Phi_1, \Phi_2, \xi)\frac{\partial V_{\text{eff}}(\Phi_1, \Phi_2, \xi)}{\partial \phi_i}, \tag{13}$$

where ξ is the gauge fixing parameter. Inspired by the gauge independence guaranteed by Nielsen identities, we employ two distinct methods for phenomenological analyses. The first approach involves calculating the finite-temperature effective potential and performing a numerical scan. The second approach focuses on determining the gauge-invariant vacuum upliftment at $T = 0$. In Sec. V, we highlight that the upliftment of the true vacuum relative to the symmetric vacuum at zero temperature serves as an effective probe of the phase transition's strength. While the first method carries uncertainties associated with gauge parameter choices, the latter approach is gauge invariant, as assured by Nielsen identities [12,51]. It is worth noting that we introduce additional counterterms at one-loop order to preserve the positions of the electroweak vacuum and masses. The agreement between our numerical scan and the profile derived from the vacuum upliftment serves to confirm the reliability of the numerical scan despite its inherent uncertainties.[3]

IV. ELECTROWEAK PHASE TRANSITION AND GRAVITATIONAL WAVES

The finite temperature effective potential dictates the phase-transition pattern. The two-Higgs doublet model displays both single and multistep phase transitions. The first-order phase transition occurs through tunneling from false to true vacua. It results in bubbles of the broken phase that pop up and expand in the surrounding region of the symmetric phase, transitioning from the false vacuum to the true vacuum. The tunneling probability is given by [60,61]

$$\Gamma(T) \approx T^4\left(\frac{S_3}{2\pi T}\right)^{3/2} e^{-\frac{S_3}{T}}, \tag{14}$$

---

[1]A renormalization group improved calculation can be taken into account for a further refined estimation [42]. For the renormalization scale μ^2 dependence of effective potential at finite temperature, we refer to Ref. [43].

[2]The first and second derivatives of the effective potential exhibit IR divergence at zero temperature as a result of the contribution from Goldstone bosons [46,47]. To address this, we use the analytical expression provided in Ref. [44] to evaluate derivatives of effective potential and compute the counterterms.

[3]For a comprehensive analysis of the uncertainties associated with finite temperature effective potential, we refer to [59].

where S_3 represents the three-dimensional Euclidean action associated with the critical bubble formation

$$S_3 = 4\pi \int_0^\infty dr\, r^2 \left[\frac{1}{2} \left(\frac{d\phi(r)}{dr} \right)^2 + V(\phi, T) \right]. \quad (15)$$

Here, the scalar field ϕ corresponds to the critical bubble profile, which is determined by solving the following differential equation:

$$\frac{d^2\phi}{dr^2} + \frac{2}{r}\frac{d\phi}{dr} = \frac{dV(\phi, T)}{d\phi}, \quad \text{with} \quad \lim_{r\to\infty} \phi(r) = 0$$

$$\text{and} \quad \lim_{r\to 0} \frac{d\phi(r)}{dr} = 0. \quad (16)$$

We utilize the publicly available code `CosmoTransitions` [62] to solve the differential equation and compute the Euclidean action S_3.

The first-order phase transition is considered to be completed around the nucleation temperature T_n, which corresponds to the point where one bubble nucleates per unit horizon volume [63],

$$\int_{T_n}^\infty \frac{dT}{T} \frac{\Gamma(T)}{H(T)^4} = 1. \quad (17)$$

This condition ensures that the bubbles percolate even in the inflating Universe. For the electroweak phase transition, with a nucleation temperature of approximately $T_n \approx 100$ GeV, this condition can be approximated as [50]

$$\frac{S_3(T)}{T} \approx 140. \quad (18)$$

To preserve the baryon asymmetry generated through electroweak baryogenesis, it is crucial to suppress the sphaleron process inside the bubble. This requires the electroweak symmetry breaking to undergo a strong first-order phase transition [50]

$$\xi_c \equiv \frac{v_c}{T_c} \gtrsim 1, \quad (19)$$

where $v_c \equiv \sqrt{\omega_1^2(T_c) + \omega_2^2(T_c) + \omega_{CB}^2(T_c)}$ is the Higgs VEV at the critical temperature T_c. This critical temperature corresponds to the point where the broken and unbroken vacua of the electroweak symmetry are degenerate. The approximate inequality in Eq. (19) indicates the theoretical uncertainty in this condition [51].

The production of stochastic gravitational waves is a significant consequence of a first-order phase transition. These GW originate from three main sources: the collision of vacuum bubbles, fluid motion resembling sound waves in the plasma, and turbulent motion within the plasma. Each source contributes to the GW spectrum, which can be described by numerical functions dependent on two

parameters that capture the dynamics of the phase transition at the nucleation temperature T_n [17,64–66].[4] The first parameter is α, defined as the ratio of the latent heat released during the phase transition (ϵ) to the energy density of the vacuum radiation ($\rho_{\rm rad}$), i.e., $\alpha \equiv \epsilon/\rho_{\rm rad}$. The latent heat and the vacuum radiation energy density are expressed as

$$\epsilon = \Delta\left(-V_{\rm eff} + T\frac{\partial V_{\rm eff}}{\partial T} \right)_{T=T_n} \quad \text{and} \quad \rho_{\rm rad} = \frac{\pi^2}{30} g_\star T_n^4, \quad (20)$$

where Δ represents the difference between the true and false vacua, and $g_\star$ the number of relativistic degrees of freedom in the plasma. The second important parameter is β/H_n, which characterizes the inverse time duration of the phase transition. This quantity is defined as[5]

$$\frac{\beta}{H_n} \equiv T_n \frac{d}{dT}\left(\frac{S_3}{T} \right)\Bigg|_{T=T_n}, \quad (21)$$

where H_n is the Hubble constant at the nucleation temperature T_n. Detectable GW signals are typically associated with a slow phase transition (small β/H_n) and a large latent heat release (large α).

Finally, to assess the detectability of GW signal, we employ the signal-to-noise ratio (SNR) measure [64]

$$\text{SNR} = \sqrt{ \mathcal{T} \int_{f_{\rm min}}^{f_{\rm max}} df \left[\frac{h^2 \Omega_{\rm GW}(f)}{h^2 \Omega_{\rm Sens}(f)} \right]^2 }, \quad (22)$$

where $\Omega_{\rm Sens}$ represents the sensitivity curve of the considered GW detector [67] and $\mathcal{T}$ corresponds to the mission duration. For our analysis, we adopt the LISA gravitational wave detector as a benchmark, with $\mathcal{T} = 5$ years and a detection threshold of SNR $= 10$ [64].

The existence of percolation temperature T_p, where 29% of space is covered by bubbles, guarantees the completion of phase transition [68]. Supercooling emerges when the nucleation temperature is substantially lower than the critical temperature, leading to a pronounced $\alpha \gg 1$ [68,69]. In our analysis, the overwhelming majority of data points in our scan, specifically 99.99%, display $\alpha < 1$. Hence, we assume there is no supercooling and the percolation temperature can be approximated to the nucleation temperature $T_p \simeq T_n$.

V. BARRIER FORMATION AND VACUUM UPLIFTMENT

Introducing a second Higgs doublet to the SM Higgs sector can alter the behavior of electroweak symmetry

---

[4]Comprehensive information on the computation of gravitational wave signals can be found in Appendix B.

[5]The derivative $\frac{d}{dT}\left(\frac{S_3}{T}\right)$ is calculated using the fourth-order finite difference formula with $\Delta T = 0.01$ GeV.
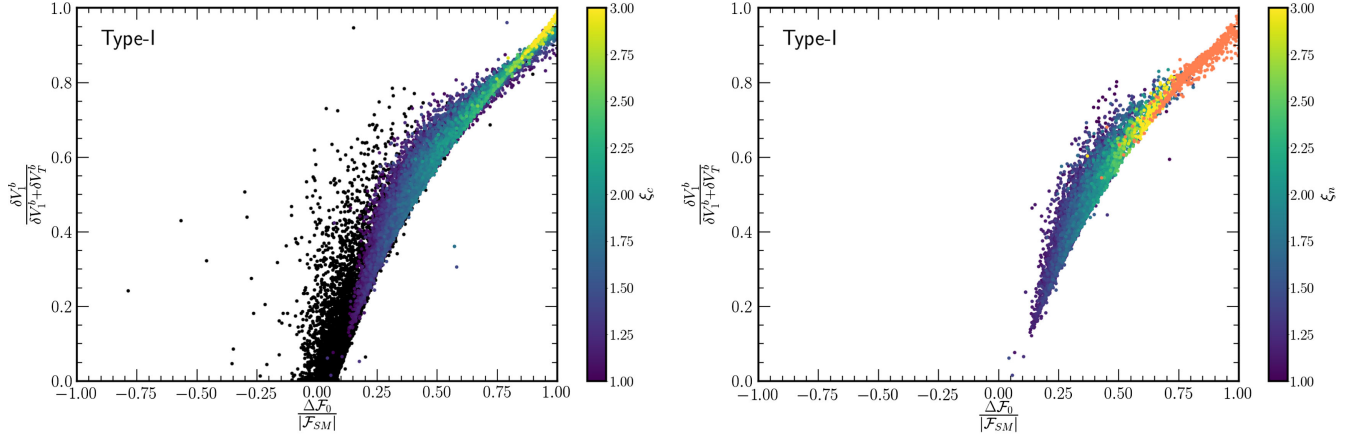
FIG. 1. The ratio $\frac{\delta V_1^b}{\delta V_1^b + \delta V_T^b}$ for the barrier at T_c versus $\Delta\mathcal{F}_0/\mathcal{F}_0^{\text{SM}}$ color coded with ξ_c. Black denotes all first-order phase transition points with $0 < \xi_c < 1$. In the right panel, we have the very same $\frac{\delta V_1^b}{\delta V_1^b + \delta V_T^b}$ for the barrier at T_c versus $\Delta\mathcal{F}_0/\mathcal{F}_0^{\text{SM}}$ color coded with ξ_n for the parameter points that have a solution to Eq. (18), thereby they have a nucleation temperature. The orange points represent parameter space configurations where the Universe is trapped in the false vacuum and the phase transition is incomplete. In these plots, we only considered the parameter points where the barrier is generated by one-loop and thermal corrections $\delta V_1^b, \delta V_T^b > 0$, which covers 99% of the parameter space points.

breaking from a smooth crossover to a strong first-order phase transition. In Ref. [15], the authors studied the key ingredients that trigger this transmutation in the EWPT by focusing on the barrier formation and upliftment of the true vacuum in the context of CP-conserving 2HDM [12–15]. In this model, the barrier is driven primarily by one-loop corrections and ξ_c can be correlated with $\Delta\mathcal{F}_0/\mathcal{F}_0^{\text{SM}}$, a gauge independent parameter calculated at zero temperature. The $\Delta\mathcal{F}_0/\mathcal{F}_0^{\text{SM}}$ is defined as

$$\frac{\Delta\mathcal{F}_0}{|\mathcal{F}_0^{\text{SM}}|} \equiv \frac{\mathcal{F}_0 - \mathcal{F}_0^{\text{SM}}}{|\mathcal{F}_0^{\text{SM}}|}, \qquad (23)$$

where $\mathcal{F}_0$ is the zero-temperature vacuum energy density of the 2HDM defined as

$$\mathcal{F}_0 \equiv V_{\text{eff}}(v_1, v_2, T = 0) - V_{\text{eff}}(0, 0, T = 0), \quad (24)$$

with $\mathcal{F}_0^{\text{SM}} = -1.25 \times 10^8 \text{ GeV}^4$.

It is interesting to examine whether the phase transition features of the CP-conserving 2HDM prevail in the CP-violating 2HDM. In Fig. 1 (left panel), we show that the fraction of one-loop contribution to the barrier height is correlated with the zero-temperature vacuum upliftment measure $\Delta\mathcal{F}_0/\mathcal{F}_0^{\text{SM}}$. We observe that the larger the one-loop correction, the higher the value of vacuum upliftment. In particular, this correlation can be seen for $\xi_c \gtrsim 1$. As one-loop effects are the dominant contributions, we can use $\Delta\mathcal{F}_0/\mathcal{F}_0^{\text{SM}}$ to shed light on the properties of the EWPT. We can approximately propose $\Delta\mathcal{F}_0/\mathcal{F}_0^{\text{SM}} \gtrsim 0.2$ as minimal condition for strongly first-order EWPT in the CP-violating 2HDM.

In the scenario where the vacuum upliftment measure $\Delta\mathcal{F}_0/\mathcal{F}_0^{\text{SM}}$ is extremely large, the tunneling from false vacuum to true vacuum becomes challenging, translating into Eq. (18) having no solution [15,16]. Thus, the Universe is trapped in a high energetic electroweak symmetric vacuum, yielding a nonphysical vacuum. In the Fig. 1 (right panel), we denote these points with the orange color. Most of the parameter points with vacuum upliftment measure $\Delta\mathcal{F}_0/\mathcal{F}_0^{\text{SM}} \gtrsim 0.87$ exhibit a vacuum trapped scenario. The above constraint excludes the bulk of $\xi_c > 2$ points, which would otherwise serve as promising candidates for successful electroweak baryogenesis.

In Fig. 2 (upper panel), we show the scanned points in the $(\Delta m_{H_\uparrow}, \Delta m_{H_\downarrow})$ plane color-coded by ξ_c, where $m_{H_\uparrow}$ $(m_{H_\downarrow})$ represents the mass of the heaviest (lightest) BSM neutral scalar, and $\Delta m_{H_\uparrow} \equiv m_{H^\pm} - m_{H_\uparrow}$ $(\Delta m_{H_\downarrow} \equiv m_{H^\pm} - m_{H_\downarrow})$. The gray points in the background pass all the theoretical and current experimental constraints. The black points also satisfy the first-order phase transition condition with $0 < \xi_c < 1$. The preference to the region with $m_{H_\uparrow} \approx m_{H^\pm}$ or $m_{H_\downarrow} \approx m_{H^\pm}$ is induced predominantly by electroweak precision measurements [70,71]. The $\xi_c > 1$ points favor a large value of $|\Delta m_{H_\uparrow}|$ or $|\Delta m_{H_\downarrow}|$ because a higher value of $\Delta\mathcal{F}_0/\mathcal{F}_0^{\text{SM}}$ requires a larger mass split, similarly to the CP-conserving scenario [15]. In Fig. 2 (middle panel), we present the parameter points in the $(\Delta m_{H_\uparrow}, \Delta m_{H_\downarrow})$ plane, color-coded by ξ_n. The points marked in orange correspond to locations where vacuum trapping occurs. The majority of parameter points with large values of ξ_c, where $m_{H_\uparrow} \approx m_{H^\pm}$ and $m_{H^\pm} - m_{H_\downarrow} > 250$ GeV, are trapped in the false vacuum state. As a result, the phase transition remains incomplete.
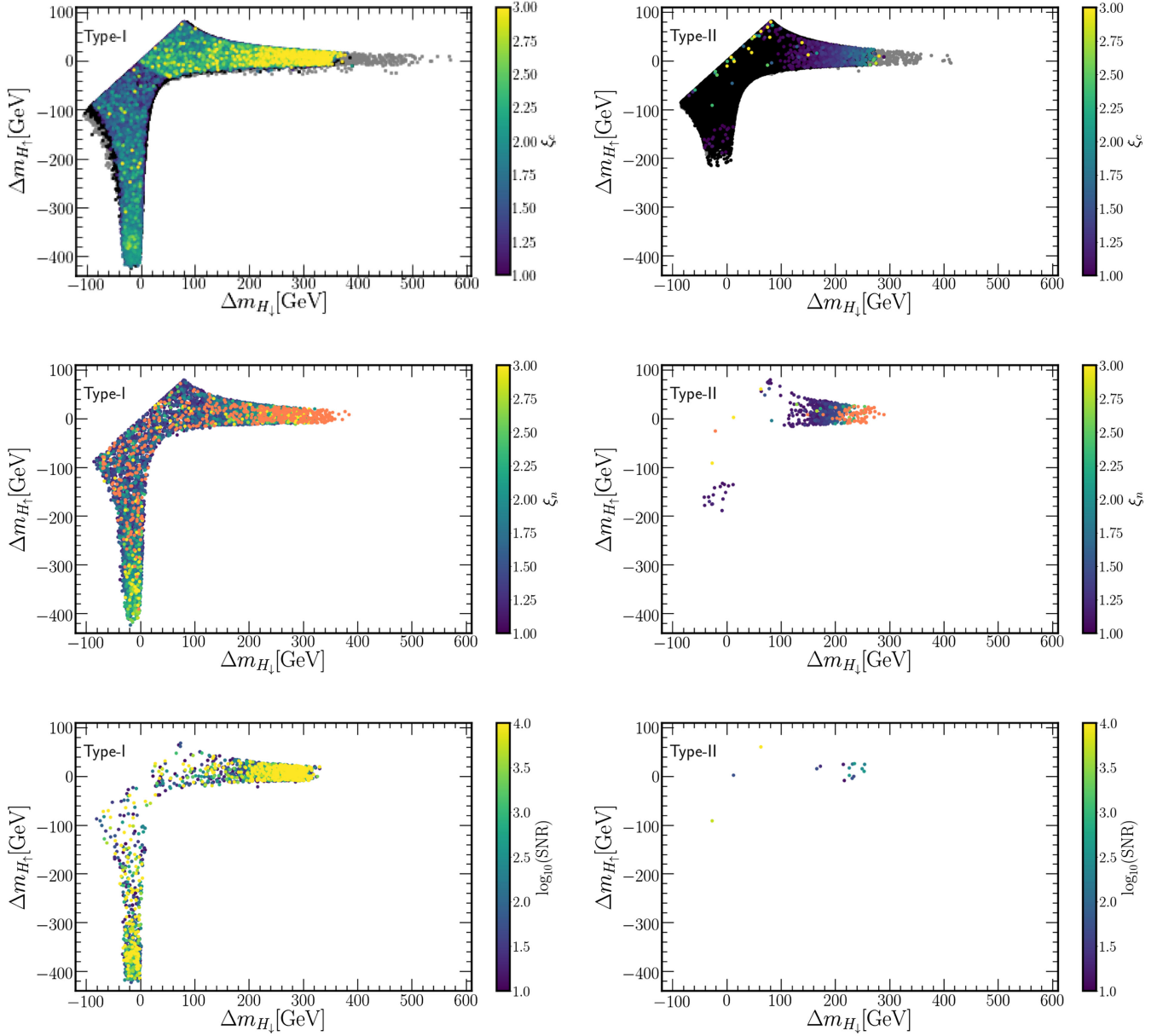
FIG. 2.   The parameter space scan in terms of $(\Delta m_{H_\uparrow}, \Delta m_{H_\downarrow})$ for Type-I (left panel) and Type-II (right panel). The heat map tracks order parameter ξ_c (upper panel), ξ_n (middle panel), and $\log_{10}(\text{SNR})$ (lower panel). The gray points in the upper panel pass all theoretical and current experimental constraints. Black points also show first-order phase transition with $0 < \xi_c < 1$. The samples with $\xi_c < 1$ have been excluded from the middle and bottom panels. In the middle panel, orange color represents parameter points trapped in false vacuum and phase transition is incomplete. The parameter space scan is implemented using ScannerS [31], where we impose the constraints from perturbative unitarity, boundedness from below, vacuum stability, electroweak precision, flavor constraints, and EDM limits. HiggsBounds and HiggsSignals are used to incorporate the searches for additional scalars as well as the 125 GeV Higgs boson measurements [38,39].

In Fig. 2 (lower panel), we show parameter points that can be probed by LISA in the $(\Delta m_{H_\uparrow}, \Delta m_{H_\downarrow})$ plane. The color coding in this case represents the logarithm (base 10) of the signal-to-noise ratio. We focus on points above the SNR threshold, SNR > 10. Among these points, we highlight the benchmark point BP4 in Table I, which serves as an example of a parameter point that can be probed by LISA. For the parameter points with $\xi_n > 1$, 6% of Type-I

points show a detectable GW signal by LISA, whereas it is around 2.5% for Type-II. These differences between Type-I and Type-II scenarios are driven by constraints from flavor physics [15]. More concretely, constraints from B-meson decays impose a lower bound on the charged scalar mass requiring $m_{H^\pm} \gtrsim 580$ GeV in the Type-II 2HDM. In Fig. 3, we show the correlation between the SNR and zero-temperature vacuum upliftment measure $\Delta\mathcal{F}_0/\mathcal{F}_0^{\text{SM}}$ for

TABLE I.   Benchmark points for the complex two-Higgs double model.

	BP1	BP2	BP3	BP4
$m_{H_\downarrow}$ (GeV)	178.596	227.340	237.815	151.408
$m_{H_\uparrow}$ (GeV)	348.814	446.822	440.556	443.706
m_{H^+} (GeV)	368.266	222.252	219.544	438.803
t_β	15.069	11.346	16.622	11.316
m_{12}^2 (GeV^2)	4471.227	23658.001	3837.544	2043.461
α_c	-0.1816	-0.0030	-0.2404	-0.0410
$\cos(\beta - \alpha)$	0.2628	0.2129	0.1544	0.1316
ξ_c	1.575	1.161	1.519	2.13
T_c (GeV)	128.65	127.54	120.24	106.65
T_n (GeV)	121.04	127.22	116.81	80.78
α	0.0227	0.0142	0.0262	0.0642
β/H_n	2.488×10^3	1.490×10^6	7.186×10^3	4.744×10^2
SNR	2.73×10^{-1}	3.01×10^{-13}	9.72×10^{-3}	1.09×10^4
η_B^{tun}	5.51×10^{-12}	1.09×10^{-10}	1.16×10^{-12}	1.43×10^{-13}
η_B^{Kink}	1.06×10^{-11}	8.79×10^{-14}	-2.33×10^{-12}	4.10×10^{-13}

the Type-I parameter points with $\xi_n > 1$. The bulk of parameter points that exhibit strong GW signals are associated with large $\Delta\mathcal{F}_0/\mathcal{F}_0^{\text{SM}}$ measure. In most cases, parameter points with $\Delta\mathcal{F}_0/\mathcal{F}_0^{\text{SM}} < 0.4$ do not show a promisable GW at LISA.

VI. BARYON ASYMMETRY CALCULATION

A. Estimation of bubble wall profile

The bubble profile in the radial coordinate can be obtained by solving the tunneling equation, Eq. (16). The baryon asymmetry calculation is performed in the bubble wall coordinate system z, where $z = 0$ denotes the bubble wall. We obtain the position of the bubble wall in the radial coordinate system r_0, where the energy density obtains the maximum value. The energy density U_E is given by
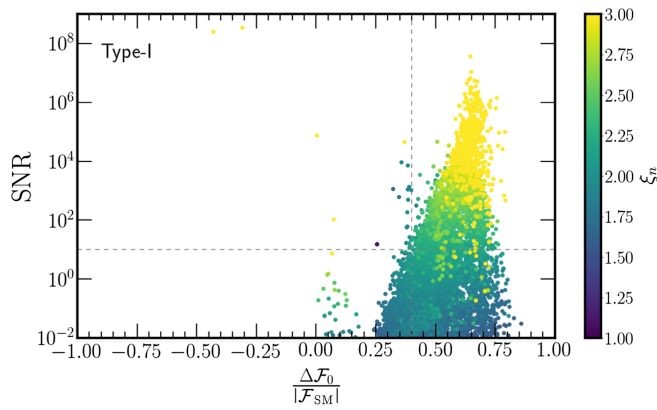

FIG. 3.   SNR versus $\Delta\mathcal{F}_0/\mathcal{F}_0^{\text{SM}}$ color coded with ξ_n for the Type I parameter point with $\xi_n > 1$. The dotted line in the plot corresponds to an SNR value of 10, serving as the threshold above which LISA can probe the parameter points.

$$U_E(r) = \frac{1}{2}[\phi'(r)]^2 + V_{\text{eff}}(\phi(r)), \qquad (25)$$

and the bubble wall coordinate z can be defined as

$$z = r - r_0. \qquad (26)$$

A key ingredient for the baryogenesis is the complex mass of quarks and leptons, which couples to Φ_2,

$$m_i(z) = \frac{y_i}{\sqrt{2}}\omega_2 e^{-i\omega_\theta} \equiv |m_i(z)|e^{i\theta^i(z)}. \qquad (27)$$

To illustrate these concepts, we present a graphical representation in Fig. 4. The left panel displays the energy density $U_E(r)$ as a function of the radial distance r, specifically for benchmark point BP1 as defined in Table I. The position of the bubble wall is identified as the barrier of the tunneling profile. On the right panel, we show the dynamic variation of the CP-violating angle of the top quark with respect to temperature in the broken phase for the BP1. As thermal effects come into play, additional CP violation is induced at higher temperatures. This effect becomes prominent, whereas at zero temperature, it is roughly seven orders of magnitude smaller. The oscillatory behavior observed between temperatures of 20 GeV and 35 GeV arises due to thermal contributions that lead to a change in sign of the CP angle, which we represent in terms of the absolute value $|\theta_t|$.

In the literature, it is a customary practice to parameterize the tunneling profile $\theta^i(z)$ by the kink profile [20–24]

$$\theta^i(z) = \frac{\theta_{\text{brk}}^i + \theta_{\text{sym}}^i}{2} - \frac{\theta_{\text{brk}}^i - \theta_{\text{sym}}^i}{2}\tanh\left(\frac{z}{L_W}\right), \quad (28)$$
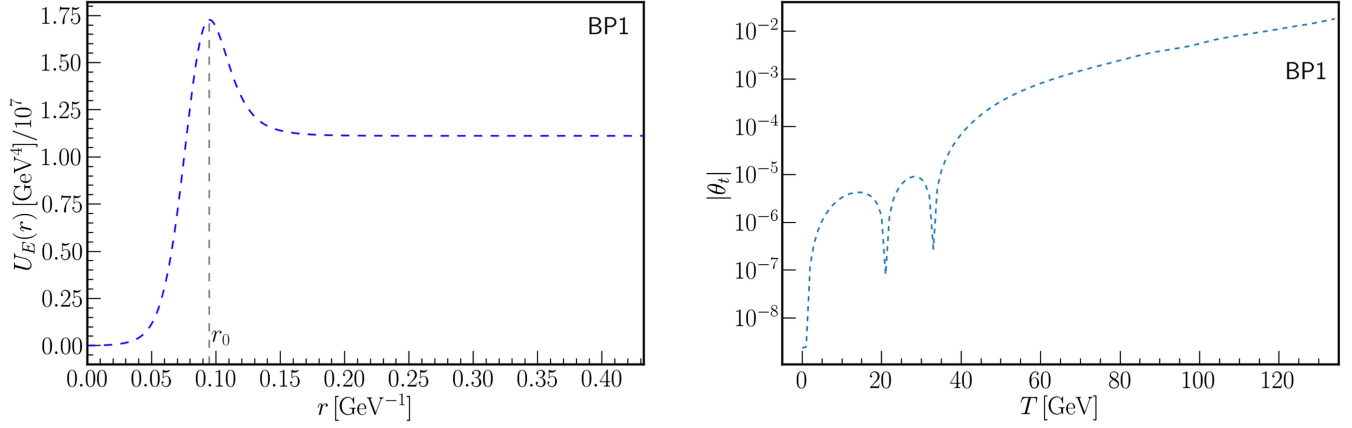
FIG. 4. The left panel shows energy density $U_E(r)$ as a function of r for BP1 as defined in Table I. The position of the bubble wall r_0 is determined as maxima of $U_E(r)$. In the right panel, we show the dynamic evaluation of the CP-violating angle of the top quark θ_t with temperature in the broken phase.

where $\theta^i_{\rm brk}$ ($\theta^i_{\rm sym}$) is the phase at the broken (symmetric) minimum. The thickness of the wall L_W is given by $L_W = v_n/\sqrt{8V_b}$ [21] with v_n representing the VEV at EWPT and V_b the height of the barrier that separates the two minima (at the nucleation temperature T_n). Remarkably, this parametrization displays a tunneling profile that is symmetric with respect to the bubble wall. In Sec. VII, we compare the estimation of the baryon asymmetry of the Universe using two different methods; the kink profile and the explicit solution from the bubble profile. In the latter case, the bubble profile is obtained by directly solving the tunneling equation. By comparing the results obtained from these two approaches, we can evaluate the consistency and reliability of the BAU estimation.

B. Semiclassical force method

The baryon asymmetry in the Universe can be estimated using the semiclassical force method. This framework utilizes the existence of a fermion with varying complex mass as it passes through the bubble wall. The particle interaction with the bubble wall can be formalized using the WKB approximation [21,22,72] or the closed-time-path formalism of thermal field theory [73–76], where the force acting on the particle is given by

$$F_z = -\frac{(m^2)'}{2E_0} \pm s\frac{(m^2\theta')'}{2E_0E_{0z}} \mp \frac{\theta'm^2(m^2)'}{4E_0^3E_{0z}}. \qquad (29)$$

The radial coordinate denotes the perpendicular distance from the wall in the rest frame of the wall, where the positive direction of z points towards the symmetric phase. E_0 is the conserved-wall frame energy of the quasiparticle, $E_{0z}^2 = E_0^2 - p_\parallel^2$ and $(..)'$ denotes the derivative with respect to the z coordinate. The first term in Eq. (29) conserves CP, whereas the second and third terms depend on the spin and nature of the particle, with the upper sign solution

corresponding to the particle and the lower sign to the antiparticle. Thus, the presence of a nonzero value for θ' generally indicates the appearance of CP violation [21,22,74]. Assuming that the kinetic momentum is conserved in collisions, the perturbation δf_i from the equilibrium density f_i of species i caused by the movement of the bubble wall is given by

$$f_i = \frac{1}{e^{\beta[\gamma_W(E_0+v_wp_z)-\mu_i]} \pm 1} + \delta f_i, \qquad (30)$$

where $\beta = 1/T, \gamma_W = 1/\sqrt{1-v_w^2}$ is the boost factor of the wall, and $+(-)$ refers to fermions (bosons).

In Eq. (29), the CP-even term is first order in derivatives, while the CP-odd term is second order in derivatives; thus we can solve the CP-even and -odd parts separately. Following Ref. [24], we introduce the following definition

$$\mu_i \equiv \mu_{i,1e} + \mu_{i,2o} + \mu_{i,2e}, \quad \delta f_i \equiv \delta f_{i,1e} + \delta f_{i,2o} + \delta f_{i,2e}. \qquad (31)$$

The evolution of f_i is described by the Boltzmann equation

$$\mathbf{L}[f_i] \equiv (v_g\partial_z + \dot{p}_z\partial_{p_z})f_i = C[f_i], \qquad (32)$$

where $\mathbf{L}[f_i]$ is the Liouville operator and v_g is the group velocity determined by WKB dispersion relation [22]

$$v_g = \frac{P_z}{E_0}\left(1 \pm \frac{\theta'm^2}{2E_0^2E_{0z}}\right). \qquad (33)$$

The $C[f_i]$ is a model-dependent collision integral associated with the interaction rate of the thermal bath [77]. The terms in the fluid equation can be written as the average overphase space of the form [21,24]

$$\langle X \rangle = \frac{\int d^3p\, X(p)}{\int d^3p\, f'_{0+}(m=0)}, \qquad \left\langle \frac{p_z}{E_0} X \right\rangle = \frac{\int d^3p\, \frac{p_z}{E_0} X(p)}{\int d^3p\, f'_{0+}(m=0)}, \tag{34}$$

where $f'_{0+}(m=0)$ can be written as

$$f'_{0+}(m=0) \equiv f_i|_{\text{fermion},\mu_i=0,\delta f_i=0,v_W=0}. \tag{35}$$

Plasma velocities can be defined as

$$u_i \equiv \left\langle \frac{p_z}{E_0} \delta f_i \right\rangle. \tag{36}$$

The second-order CP-odd chemical potential is defined by the difference between the second-order chemical potential of the particle and its antiparticle, and a similar definition follows for corresponding plasma velocities,

$$\mu_{i,2} \equiv \mu_{i,2o} - \bar{\mu}_{i,2o}, \qquad u_{i,2} \equiv u_{i,2o} - \bar{u}_{i,2o}. \tag{37}$$

The zeroth and first momenta of the collision integral can be written in terms of inelastic rate Γ_{inel} and total interaction rate Γ_{tot} by [77]

$$\langle C[f_i] \rangle = \Gamma_{\text{inel}} \sum \mu_i, \qquad \left\langle \frac{p_z}{E_0} C[f_i] \right\rangle = -\Gamma_{\text{tot}} u. \tag{38}$$

For the generation of the baryon asymmetry, the first step is to produce asymmetry in left-handed quarks. We consider the effects of the strong sphaleron process, W-scattering, top Yukawa interaction, helicity flip, and Higgs number violation with the rate of Γ_{ss}, Γ_W, Γ_y, Γ_m, and Γ_h, respectively. The last two processes are relevant only in the broken phase. The transport equation for chemical potentials of the left-handed top quark, the conjugate of the right-handed bottom quark, left-handed bottom quark, Higgs bosons, and the corresponding plasma velocities are given as follows [21,22,24]:

(i) Left-handed top quarks (t)

$$0 = 3v_w K_{1,t}(\partial_z \mu_{t,2}) + 3v_w K_{2,t}(\partial_z m_t^2)\mu_{t,2} + 3(\partial_z u_{t,2}) - 3\Gamma_y(\mu_{t,2} + \mu_{t^c,2} + \mu_{h,2})$$
$$- 6\Gamma_M(\mu_{t,2} + \mu_{t^c,2}) - 3\Gamma_W(\mu_{t,2} - \mu_{b,2}) - 3\Gamma_{ss}[(1+9K_{1,t})\mu_{t,2} + (1+9K_{1,b})\mu_{b,2}$$
$$+ (1-9K_{1,t})\mu_{t^c,2}], \tag{39}$$

$$S_t = -3K_{4,t}(\partial_z \mu_{t,2}) + 3v_w \tilde{K}_{5,t}(\partial_z u_{t,2}) + 3v_w \tilde{K}_{6,t}(\partial_z m_t^2)u_{t,2} + 3\Gamma_t^{\text{tot}} u_{t,2}. \tag{40}$$

(ii) Charge conjugation of right-handed top quarks (t^c)

$$0 = 3v_w K_{1,t}(\partial_z \mu_{t^c,2}) + 3v_w K_{2,t}(\partial_z m_t^2)\mu_{t^c,2} + 3(\partial_z u_{t^c,2}) - 3\Gamma_y(\mu_{t,2} + \mu_{b,2} + 2\mu_{t^c,2} + 2\mu_{h,2})$$
$$- 6\Gamma_M(\mu_{t,2} + \mu_{t^c,2}) - 3\Gamma_{ss}[(1+9K_{1,t})\mu_{t,2} + (1+9K_{1,b})\mu_{b,2} + (1-9K_{1,t})\mu_{t^c,2}], \tag{41}$$

$$S_t = -3K_{4,t}(\partial_z \mu_{t^c,2}) + 3v_w \tilde{K}_{5,t}(\partial u_{t^c,2}) + 3v_w \tilde{K}_{6,t}(\partial_z m_t^2)u_{t^c,2} + 3\Gamma_t^{\text{tot}} u_{t^c,2}. \tag{42}$$

(iii) Left-handed bottom quarks (b)

$$0 = 3v_w K_{1,b}(\partial_z \mu_{b,2}) + 3(\partial_z u_{b,2}) - 3\Gamma_y(\mu_{b,2} + \mu_{t^c,2} + \mu_{h,2}) - 3\Gamma_W(\mu_{b,2} - \mu_{t,2})$$
$$- 3\Gamma_{ss}[(1+9K_{1,t})\mu_{t,2} + (1+9K_{1,b})\mu_{b,2} + (1-9K_{1,t})\mu_{t^c,2}], \tag{43}$$

$$0 = -3K_{4,b}(\partial_z \mu_{b,2}) + 3v_w \tilde{K}_{5,b}(\partial_z u_{b,2}) + 3\Gamma_b^{\text{tot}} u_{b,2}. \tag{44}$$

(iv) Higgs

$$0 = 4v_w K_{1,h}(\partial_z \mu_{h,2}) + 4(\partial_z u_{h,2}) - 3\Gamma_y(\mu_{t,2} + \mu_{b,2} + 2\mu_{t^c,2} + 2\mu_{h,2}) - 4\Gamma_h \mu_{h,2}, \tag{45}$$

$$0 = -4K_{4,h}(\partial_z \mu_{h,2}) + 4v_w \tilde{K}_{5,h}(\partial_z u_{h,2}) + 4\Gamma_h^{\text{tot}} u_{h,2}. \tag{46}$$

S_t denotes the source term of the top quark that can be written as

$$S_t = -v_W K_{8,t} \partial_z(m_t^2 \partial_z \theta) + v_W K_{9,t}(\partial_z \theta)m_t^2(\partial_z m_t^2). \tag{47}$$

The source term for the bottom quark can be neglected due to the suppression factor $m_b^2/m_t^2 \sim 10^{-3}$. Thermal transport coefficients are defined as

$$K_{1,i} = -\left\langle \frac{p_z^2}{E_0^2} \partial_E^2 f_{i,0} \right\rangle, \qquad K_{2,i} = \left\langle \frac{\partial_E^2 f_{i,0}}{2E_0} \right\rangle, \quad (48a)$$

$$K_{4,i} = \left\langle \frac{p_z^2}{E_0^2} \partial_E f_{i,0} \right\rangle, \qquad \tilde{K}_{5,i} = \left[\frac{p_z^2}{E_0^2} \partial_E f_{i,0} \right], \quad (48b)$$

$$\tilde{K}_{6,i} = \left[\frac{E_0^2 - p_z^2}{2E_0^3} \partial_E f_{i,0} \right], \quad K_{8,i} = \left\langle \frac{|p_z|\partial_E f_{i,0}}{2E_0^2 E_{0z}} \right\rangle, \quad (48c)$$

$$K_{9,i} = \left\langle \frac{|p_z|}{4E_0^3 E_{0z}} \left(\frac{\partial_E f_{i,0}}{E_0} - \partial_E^2 f_{i,0} \right) \right\rangle, \quad (48d)$$

with the expectation values given by

$$\langle X \rangle = \frac{\int d^3 p X(p)}{\int d^3 p \partial_E f_{0+}(m=0)},$$

$$[X] = \frac{\int d^3 p X(p)}{\int d^3 p f_{i,0,v_W}} = \frac{\int d^3 p X(p)}{\int d^3 p f_{i,0}|_{v_W=0}}, \quad (49)$$

and the distribution function defined as

$$f_{i,0} = f_i|_{\mu_i=0,\delta f_i=0,v_w=0}, \quad f_{0+} = f_i|_{\text{fermion},\mu_i=0,\delta f_i=0,v_w=0},$$

$$f_{i,0,v_w} = f_{i,0} + v_W p_z \partial_{E_0} f_{i,0}. \quad (50)$$

The third equation in Eq. (50) is a Taylor expansion; hence, it is valid only for small bubble wall velocity v_W. We assume $v_W = 0.1$. The transport equation with full dependence on the wall velocity is provided in Ref. [72]. The values for the strong sphaleron rate, top Yukawa rate, Higgs number violating rate and rate for spin-helicity flipping rate for the top quark are given by [21,24,78,79]

$$\Gamma_{ss} = 4.9 \times 10^{-4} T, \qquad \Gamma_y = 4.2 \times 10^{-3} T,$$

$$\Gamma_m = \frac{m_t^2(z,T)}{63T}, \qquad \Gamma_h = \frac{m_W^2(z,T)}{50T}, \quad (51)$$

where z is the distance. The W exchange rate can be approximated as the total Higgs interaction $\Gamma_W = \Gamma_h^{\text{tot}}$.

Finally, the asymmetry in left-handed quarks is converted into baryon asymmetry by electroweak sphaleron transition which can be calculated as [77]

$$\eta_B = \frac{n_B}{s} = \frac{405\Gamma_{ws}}{4\pi^2 v_W g_\star T} \int_0^\infty dz \mu_{B_L} \exp\left(-\frac{45\Gamma_{ws}z}{4v_W}\right), \quad (52)$$

where $\Gamma_{ws} \simeq 1 \times 10^{-6} T$ is the weak sphaleron rate estimated by lattice calculation [80] and $g_\star \simeq 106.75$ is the

effective degrees of freedom at the electroweak scale. The chemical potential for left-handed quarks μ_{B_L} is given by

$$\mu_{B_L} = \frac{1}{2}(1 + 4K_{1,t})\mu_t + \frac{1}{2}(1 + 4K_{1,b})\mu_b - 2K_{1,t}\mu_{t^c}. \quad (53)$$

We solved the top transport equation and estimate the baryon asymmetry of the Universe with BSMPT v2 [23].[6]

VII. BARYON ASYMMETRY IN THE C2HDM

In this section, we estimate the baryon asymmetry generated via electroweak baryogenesis using the semiclassical force method. A key ingredient in this calculation is the estimation of the bubble profile. As discussed in Sec. VI A, it is usual in the literature to parametrize bubble profile by the kink profile [20–22,24]. In this section, in addition to deriving the BAU in the C2HDM framework, we pay close attention to the viability of the kink profile by comparing it with the bubble profile obtained by explicitly solving the tunneling equation using CosmoTransitions [62].

In Fig. 5, we compare the magnitude of baryon asymmetry estimated using these two bubble profiles at the nucleation temperature with the color code representing the distribution probability. First, we observe that the C2HDM can satisfy the observed baryon asymmetry, matching the observed value η_{obs}. However, these points are rare in our parameter space scan. We highlight one of these points in Fig. 5 as benchmark point 2 (BP2) and detailed define it in Table I.[7] Second, we observe in Fig. 5 that for most of the points in the parameter space, the kink-profile solution leads to larger values than the profile obtained by solving the tunneling equation. In addition, there is a non-negligible fraction of points where the kink profile overestimates the asymmetries by a few orders of magnitude in comparison to the profile from the solution of the tunneling equation.

---

[6]We used CosmoTransitions to implement effective potential and calculate T_c, T_n, and tunneling profile as mentioned in Sec. IV. Currently, BSMPT does not provide a framework to compute T_n and tunneling profile. We used T_n and tunneling profile as input to BSMPT to solve the transport equation and compute the baryon asymmetry.

[7]The VEV-insertion approximation (VIA) [81] has been found to produce baryon asymmetry values that are two to three orders of magnitude larger than the semiclassical force method adopted in the current study [24], displaying a larger number of points satisfying η_{obs}. Several works have raised criticisms about the validity of the approximations used in this alternative method. One particular argument is that the expansion utilized in deriving the source term for the top quark in the VIA approach may encounter limitations due to the substantial mass of the top quark [24,72]. It is important to highlight that recent improvements have been made in treating the source term in the VIA method [82].
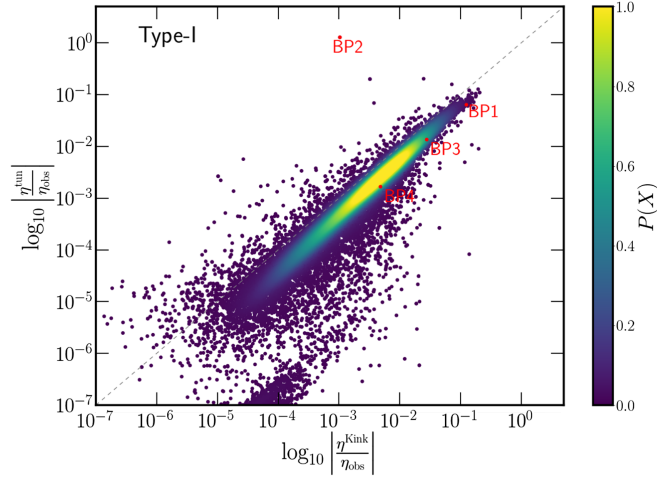
FIG. 5. Comparison of the magnitude of baryon asymmetry computed using the profile from the solution of the tunneling equation and the kink profile at T_n color coded with the probability distribution. The red color denotes the benchmark points presented in Table I.

In most cases, we can understand the difference in asymmetry using two profiles by looking at the behavior of the source term Eq. (47) in front of the bubble wall. Specifically, the sign of $\partial_z\theta_t$ in front of the bubble wall determines the sign of the source term S_t, thereby influencing the overall asymmetry. In most cases, a negative (positive) $\partial_z\theta_t$ results in a positive (negative) source term S_t, leading to a positive (negative) asymmetry. The kink profile typically provides a higher value for the top mass around the bubble wall, and thereby a higher magnitude for the source term in Eq. (47). This feature is illustrated in Fig. 6 using our benchmark point 1 (BP1) as defined in Table I. Even when the change in phase of the top mass θ_t has a larger magnitude for the tunneling profile, the value of the top mass is higher for the kink profile, and subsequently, the kink profile has a larger asymmetry. Therefore, the behavior of the top mass is the dominant factor in estimating the magnitude of the asymmetry compared to the phase of top mass θ_t.
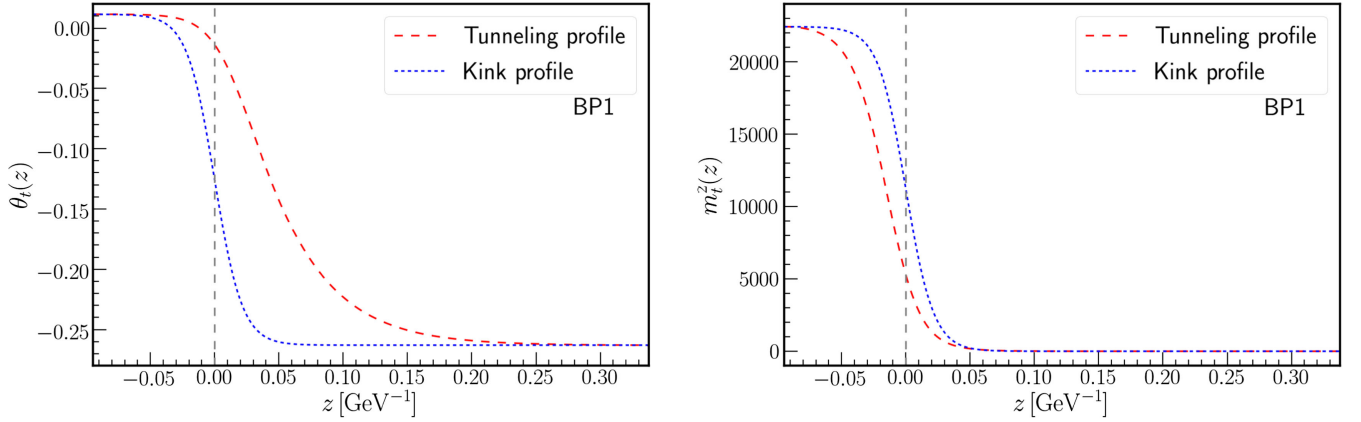

FIG. 6. Evolution of the phase of the top mass θ_t and the square of the top mass with the wall distance for the BP1, as defined in Table I. The value of the top mass near the bubble wall is larger for the kink profile, thereby leading to a larger value of asymmetry.
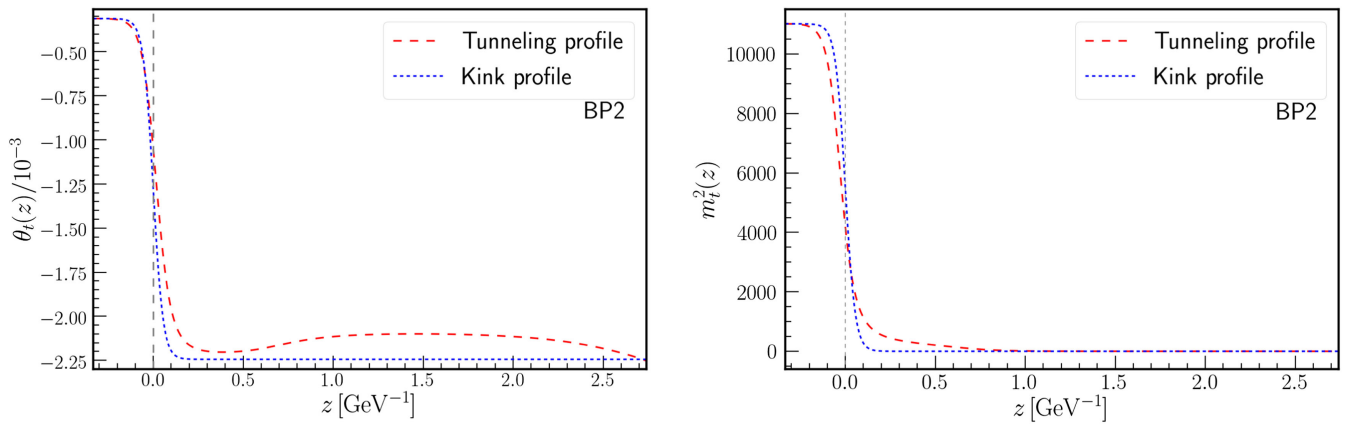

FIG. 7. The evolution of phase of top mass θ_t and square of top mass with the wall distance for the BP2. It takes a larger wall distance z for the top mass value to drop to zero in the tunneling profile compared to the kink profile. This translates into the source term being active for a larger distance and, subsequently, the larger value of asymmetry for the tunneling profile compared to the kink profile.
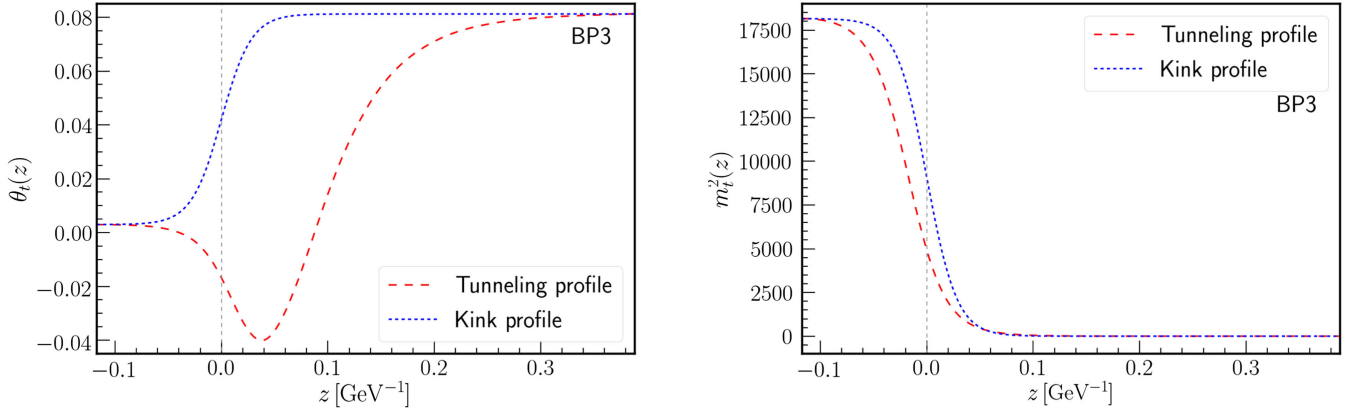
FIG. 8. The evolution of phase of top mass θ_t and square of top mass with the wall distance for the BP3. The phase of top mass near the bubble wall is an increasing function for the kink profile and decreasing function for the tunneling profile; subsequently, both asymmetries have opposite signs.

There are instances where the top mass in the tunneling profile is smaller, but does not quickly drop to zero compared to the kink profile. This translates into the source term being active for a larger wall distance for the tunneling profile compared to the kink profile. In this case, the magnitude of asymmetry calculated using the tunneling profile would have a larger value compared to the kink profile. The above feature is illustrated in the case of BP2 shown in Fig. 7, where the asymmetry differs by two orders. Once again, we highlight that BP2 can explain the value of the observed baryon asymmetry η_{obs} when using the explicit solution for the tunneling equation. The above characteristic of the tunneling profile will permit significant baryon asymmetry even though the change in CP-violating phase is relatively small.

Finally, there are instances where even the sign of the derivative for the CP phase $\partial_z \theta_t$ near the bubble wall differs between the kink and tunneling profiles. We illustrate this scenario with the benchmark point 3 (BP3) presented in Fig. 8. Near the bubble wall, θ_t exhibits an increasing trend for the kink profile, while it displays a decreasing trend for the explicit solution for the tunneling profile. Consequently, the asymmetry is positive for the tunneling profile and negative for the kink profile, despite both profiles having identical endpoints. These findings emphasize the importance of accurately determining the bubble profile and highlight the discrepancies that can arise when relying on the kink profile approximation.

VIII. SUMMARY

In this work, we explored the phase transition pattern and the feasibility of generating the observed baryon asymmetry of the Universe within the C2HDM framework while considering the theoretical and experimental constraints. First, we carefully examined the essential elements in the shape of the Higgs potential, specifically focusing on the

formation of the barrier and the upliftment of the true vacuum state. These factors are critical in facilitating the phase transition from a smooth crossover to a strong first-order phase transition. We observe that the intensity of the phase transition is linked to the elevation of the true vacuum relative to the symmetric vacuum state at zero temperature [12–15]. This phenomenon occurs due to the prevalence of one-loop effects over thermal corrections, particularly when $\xi_c > 1$ [15]. However, if the vacuum upliftment measure is too large, the Universe becomes trapped in the false vacuum state, rendering no solution for the nucleation temperature Eq. (18). This leads to parameter points with $\Delta \mathcal{F}_0 / |\mathcal{F}_0^{\mathrm{SM}}| \gtrsim 0.87$ unphysical, which excludes most of the $\xi_c > 2$ points [15,16]. Therefore, in electroweak baryogenesis studies, it is crucial to look at the nucleation temperature T_n and not just at the critical temperature T_c.

When it comes to gravitational wave signals, only a small fraction of the parameter points in the strong first-order electroweak phase-transition parameter space of the C2HDM can be probed by LISA. However, among the accessible points, those with a higher value of the ξ_c parameter display particularly strong gravitational wave signals. Notably, the Type-I parameter space points generally offer more promising gravitational wave signals compared to the Type-II parameter points in the C2HDM. These differences can be traced to the more stringent flavor constraints imposed on the Type-II scenario that shape the parameter space.

We note that the C2HDM can describe the observed baryon asymmetry η_{obs}, albeit for a limited set of parameter space points. One specific point, BP2, was highlighted as a benchmark that satisfied the observed asymmetry value. Furthermore, we contrast the impact on the baryon asymmetry calculation using two different approaches to describe the bubble profile, namely the usually adopted kink profile parametrization and the explicit solution for the tunneling equation. Our objective

was to access the dependency of the resulting value of η_B on these two approaches and evaluate their respective contributions to the baryon asymmetry calculation. We found that the majority of points in our parameter space scan yield similar results from both approaches. Nonetheless, a non-negligible portion of points exhibits significant discrepancies between these two methods. Specifically, the kink profile approximation often displays higher asymmetry values compared to the explicit solution obtained from the tunneling equation. In some cases, the discrepancy was by several orders of magnitude. The difference in the asymmetry value for the two profiles was scrutinized in terms of the behavior of the source term in front of the bubble wall.

Undoubtedly, the task of achieving a baryon asymmetry of the Universe that aligns with the observed value poses significant challenges. The requirements of a strong first-order electroweak phase transition, substantial *CP* violation, and stringent theoretical and experimental constraints make the generation of a compatible BAU a formidable task. However, the discrepancies observed in calculations performed using different profile assumptions provide avenues for improving the accuracy of computing the BAU. The comparison between the kink profile and the explicit solution for the tunneling profiles provided valuable insights into the estimation of baryon asymmetry, emphasizing the importance of accurately determining the bubble profile for a more robust analysis of electroweak baryogenesis.

APPENDIX A: PARAMETRIZATION FOR C2HDM SCAN

In this appendix, we present the detailed parametrization for the C2HDM adopted in our parameter space scan in Eq. (6). From the following minimization conditions at zero temperature

$$\frac{dV}{d\omega_1} = \frac{\omega_1(2m_{11}^2 + \lambda_1\omega_1^2 + (\lambda_5^r c_{2\omega_\theta} - \lambda_5^i s_{2\omega_\theta})\omega_2^2 + (\lambda_3 + \lambda_4)\omega_2^2) - 2m_{12}^2\omega_2 c_{\omega_\theta}}{2} = 0, \tag{A1a}$$

$$\frac{dV}{d\omega_2} = \frac{\omega_2(2m_{22}^2 + \lambda_2\omega_2^2 + (\lambda_5^r c_{2\omega_\theta} - \lambda_5^i s_{2\omega_\theta})\omega_1^2 + (\lambda_3 + \lambda_4)\omega_1^2) - 2m_{12}^2\omega_1 c_{\omega_\theta}}{2} = 0, \tag{A1b}$$

$$\frac{dV}{d\omega_\theta} = \frac{\omega_1\omega_2(2m_{12}^2 s_{\omega_\theta} - \omega_1\omega_2(\lambda_5^r s_{2\omega_\theta} + \lambda_5^i c_{2\omega_\theta}))}{2} = 0, \tag{A1c}$$

we can write the tree-level parameters as

$$m_{11}^2 = \frac{m_{12}^2 t_\beta c_\theta}{c_{2\theta}} - \frac{1}{2}v^2(c_\beta^2\lambda_1 + s_\beta^2(\lambda_3 + \lambda_4 + \lambda_5^r/c_{2\theta})), \tag{A2a}$$

$$m_{22}^2 = \frac{m_{12}^2 c_\theta}{t_\beta c_{2\theta}} - \frac{1}{2}v^2(s_\beta^2\lambda_2 + c_\beta^2(\lambda_3 + \lambda_4 + \lambda_5^r/c_{2\theta})), \tag{A2b}$$

$$\lambda_5^i = \frac{2m_{12}^2 s_\theta}{s_\beta c_\beta c_{2\theta} v^2} - \lambda_5^r t_{2\theta}. \tag{A2c}$$

Note that in the limit $\theta \to 0$, where α_c also goes to zero, we recover the *CP*-conserving 2HDM.

From the quadratic terms in the potential, we have the following relations for the charged scalar mass and neutral scalar mass matrix:

$$m_{H^\pm}^2 = \frac{m_{12}^2 c_\theta}{s_\beta c_\beta c_{2\theta}} - \frac{1}{2}v^2(\lambda_4 + \lambda_5^r/c_{2\theta}), \tag{A3a}$$

$$\mathcal{M}_N^2 = \begin{pmatrix} \mathcal{M}_{11}^2 & \mathcal{M}_{12}^2 & \mathcal{M}_{13}^2 \\ \mathcal{M}_{21}^2 & \mathcal{M}_{22}^2 & \mathcal{M}_{23}^2 \\ \mathcal{M}_{31}^2 & \mathcal{M}_{32}^2 & \mathcal{M}_{33}^2 \end{pmatrix}, \tag{A3b}$$

$$\mathcal{M}_{11}^2 = m_{12}^2 t_\beta c_\theta + \lambda_1 v^2 c_\beta^2, \tag{A3c}$$

$$\mathcal{M}_{22}^2 = \frac{m_{12}^2 c_\theta}{t_\beta} + \lambda_2 v^2 s_\beta^2, \tag{A3d}$$

$$\mathcal{M}_{33}^2 = \frac{m_{12}^2}{2s_\beta c_\beta c_{2\theta}}(3c_\theta - c_{3\theta}) - \frac{\lambda_5^r v^2}{c_{2\theta}}, \tag{A3e}$$

$$\mathcal{M}_{12}^2 = \mathcal{M}_{21}^2$$
$$= \frac{1}{2}\left(\frac{m_{12}^2(c_{3\theta}-3c_\theta)}{c_{2\theta}} + s_{2\beta}(\lambda_3 + \lambda_4 + \lambda_5^r/c_{2\theta})v^2\right),$$
$$\text{(A3f)}$$

$$\mathcal{M}_{13}^2 = \mathcal{M}_{31}^2 = -\frac{m_{12}^2 s_\theta}{c_\beta}, \qquad \text{(A3g)}$$

$$\mathcal{M}_{23}^2 = \mathcal{M}_{32}^2 = -\frac{m_{12}^2 s_\theta}{s_\beta}. \qquad \text{(A3h)}$$

From $m_{H^\pm}^2$ and $\mathcal{M}$, we obtain the expressions for $\lambda_{1,\dots,4}$, λ_5^r in terms of the physical parameters in Eq. (5):

$$\lambda_1 = \frac{\sum_i O_{i1}^2 m_i^2}{c_\beta^2 v^2} - \frac{m_{12}^2 t_\beta c_\theta}{c_\beta^2 v^2}, \qquad \text{(A4a)}$$

$$\lambda_2 = \frac{\sum_i O_{i2}^2 m_i^2}{s_\beta^2 v^2} - \frac{m_{12}^2 c_\theta}{t_\beta s_\beta^2 v^2}, \qquad \text{(A4b)}$$

$$\lambda_3 = \frac{\sum_i O_{i1}O_{i2} m_i^2}{s_\beta c_\beta v^2} - \frac{m_{12}^2 c_\theta}{s_\beta c_\beta v^2} + \frac{2m_{H^\pm}^2}{v^2}, \qquad \text{(A4c)}$$

$$\lambda_4 = \frac{\sum_i O_{i3}^2 m_i^2}{v^2} + \frac{m_{12}^2 c_\theta}{s_\beta c_\beta v^2} - \frac{2m_{H^\pm}^2}{v^2}, \qquad \text{(A4d)}$$

$$\lambda_5^r = -\frac{c_{2\theta}\sum_i O_{i3}^2 m_i^2}{v^2} + \frac{m_{12}^2(3c_\theta - c_{3\theta})}{s_{2\beta} v^2}, \qquad \text{(A4e)}$$

where O is the rotation matrix in Eq. (4) that diagonalizes $\mathcal{M}_N^2$, and m_i^2 for $i = 1, 2, 3$ are the mass eigenvalues of $\mathcal{M}_N^2$ and can be identified with m_h, $m_{H_\uparrow}$, and $m_{H_\downarrow}$. Note that the determinant of matrix O in Eq. (4) is -1, which is chosen such that the definition of α follows the same convention as the counterpart in CP-conserving 2HDM.[8] The parameters α_b and θ can be obtained by using $\mathcal{M}_{13}^2$ and $\mathcal{M}_{23}^2$,

$$s_{\alpha_b} = \frac{s_{2\alpha_c}(m_2^2 - m_3^2)}{2(m_1^2 - m_2^2 s_{\alpha_c}^2 - m_3^2 c_{\alpha_c}^2)t_{\alpha+\beta}}, \qquad \text{(A5a)}$$

$$s_\theta = -\frac{c_\beta}{m_{12}^2}\sum_i m_i^2 O_{i1}O_{i3}. \qquad \text{(A5b)}$$

With the three mixing angles α, α_b, and α_c, we can evaluate the rotation matrix O in Eq. (4) and subsequently obtain λ's using Eq. (A4). In this parametrization we choose β, α, and α_c as independent parameters. The remaining m_{11}^2, m_{22}^2, and λ_5^i can be calculated using Eq. (A2).

---

[8]To match the convention in ScannerS, extra permutations and multiplications will be added to the rotation matrix.

APPENDIX B: GRAVITATIONAL WAVE SIGNATURES

First-order phase transition (FOPT) in the early Universe can give rise to detectable stochastic GW signals today [64,83,84]. During FOPT, GWs are generated by bubble collision, sound waves, and magnetohydrodynamic (MHD) turbulence. The GW spectrum $\Omega_{\mathrm{GW}}(f)$ is the current GW energy density per logarithmic frequency interval per critical energy density of the Universe. That is $\int \Omega_{\mathrm{GW}} d\ln f$ is the fraction of GW energy density compared to the critical energy density of the Universe. The GW energy density can be linearly approximated as

$$\Omega_{\mathrm{GW}} h^2 = \Omega_{\mathrm{coll}} h^2 + \Omega_{\mathrm{SW}} h^2 + \Omega_{\mathrm{turb}} h^2. \qquad \text{(B1)}$$

Here, $h = H_0/100 \text{ Km/s/Mpc}$ is the dimensionless Hubble parameter as it stands today. In the following, we discuss each of the components of Eq. (B1).

1. Bubble collisions

Nucleated bubbles undergo collisions that disrupt their spherical symmetry and give rise to gravitational waves. In the $\frac{\beta}{H_n} \gg 1$ limit, this can be described well by the thin wall and envelope approximation [85,86]. In this approximation, GW is generated mainly from envelopes, and the overlapped region is neglected. The gravitational wave spectrum from bubble collision can be modeled by [87]

$$\Omega_{\mathrm{coll}} h^2 = \frac{1.67 \times 10^{-5}}{(\beta/H_\star)^2}\left(\frac{k_c \alpha}{1+\alpha}\right)^2\left(\frac{100}{g_*}\right)^{1/3}\left(\frac{0.11 v_w^3}{0.42 + v_w^2}\right)$$
$$\times \frac{3.8(f/f_{\mathrm{env}})^{2.8}}{1 + 2.8(f/f_{\mathrm{env}})^{3.8}}, \qquad \text{(B2)}$$

where k_c is the efficiency factor for the bubble collision [88]

$$k_c = \frac{0.715\alpha + \frac{4}{27}\sqrt{\frac{3\alpha}{2}}}{1 + 0.715\alpha}. \qquad \text{(B3)}$$

Taking into account the redshift of the frequency, the peak frequency of the GW spectrum from bubble collision is given by [89]

$$f_{\mathrm{env}} = \left(\frac{0.62 \times \beta/H_\star}{1.8 - 0.1 v_w + v_w^2}\right)16.5 \times 10^{-6}\left(\frac{T_n}{100 \text{ GeV}}\right)$$
$$\times \left(\frac{g_*}{100}\right)^{1/6} \text{ Hz}, \qquad \text{(B4)}$$

where first term in right side represents the peak frequency of the GW spectrum from bubble collision at T_n.

2. Sound waves

The energy released from the phase transition to the plasma can either go to heat or fluid motion. Numerical estimation shows that the energy-momentum tensor of the

fluid after bubble collision is similar to that of an ensemble of sound waves [90]. Remarkably, these sound waves serve as a notable source of gravitational waves. The gravitational wave spectrum stemming from these sound waves can be modeled by [90–92]

$$\Omega_{\text{SW}}h^2 = \frac{2.65 \times 10^{-6}}{\beta/H_\star} \left(\frac{k_s\alpha}{1+\alpha}\right)^2 \left(\frac{100}{g_*}\right)^{1/3} v_w \left(\frac{f}{f_{\text{SW}}}\right)^3$$
$$\times \left(\frac{7}{4+3(f/f_{\text{SW}})^2}\right)^{7/2} \Upsilon(\tau_{\text{SW}}), \qquad (B5)$$

where the peak frequency of the GW spectrum, accounting for the redshift factor, can be written as [89]

$$f_{\text{SW}} = \frac{1.9 \times 10^{-5}}{v_w} \left(\frac{\beta}{H_\star}\right) \left(\frac{T_n}{100\,\text{GeV}}\right) \left(\frac{g_*}{100}\right)^{1/6} \text{Hz}. \quad (B6)$$

For the radiation-dominant Universe, the lifetime of the sound waves is finite. Recent studies [93,94] show a suppression factor $\Upsilon(\tau_{\text{SW}})$ due to the finite active period τ_{SW} of sound waves

$$\Upsilon(\tau_{\text{SW}}) = 1 - \frac{1}{\sqrt{1 + 2\tau_{\text{SW}}H_\star}}, \qquad (B7)$$

where the efficiency factor for the sound wave spectrum k_s is given by [64]

$$k_s = \frac{\alpha}{0.73 + 0.083\sqrt{\alpha} + \alpha}. \qquad (B8)$$

The sound wave lasts until the turbulence starts to develop. The duration τ_{SW} is quantified with [90]

$$\tau_{\text{SW}} = \frac{R_\star}{\overline{U_f}}, \qquad (B9)$$

where $R_\star \simeq (8\pi)^{1/3} v_w/\beta$ denotes the mean bubble separation and $\overline{U_f}^2$ represents the mean square velocity [95]

$$\overline{U_f}^2 = \frac{3}{4}\frac{\alpha}{1+\alpha}k_s. \qquad (B10)$$

3. MHD turbulence

The energy injected into the plasma can induce turbulence in the fluid if the early Universe plasma has an extremely high Reynolds number [88]. This turbulent motion can be a source of gravitational waves [96]. Additionally, a fully ionized plasma can give rise to a turbulent magnetic field under turbulent motion, leading to GWs. The GW spectrum stemming from turbulence can be parametrized as [97]

$$\Omega_{\text{turb}}h^2 = \frac{3.35 \times 10^{-4}}{\beta/H_\star} \left(\frac{k_t\alpha}{1+\alpha}\right)^{3/2} \left(\frac{100}{g_*}\right)^{1/3} v_w \left(\frac{f}{f_{\text{SW}}}\right)^3$$
$$\times \frac{1}{[1 + (f/f_{\text{turb}})]^{11/3}(1 + 8\pi f/h_\star)}, \qquad (B11)$$

where $h_\star$ is the factor accounting redshift of the frequency

$$h_\star = 16.5 \times 10^{-6} \left(\frac{T_n}{100\,\text{GeV}}\right) \left(\frac{g_*}{100}\right)^{1/6} \text{Hz}. \quad (B12)$$

Based on insights drawn from numerical simulation, we adopt $k_{\text{turb}} = 0.05k_s$ [64]. Finally, the peak frequency for GW spectrum arising from MHD turbulence can be written as [97],

$$f_{\text{turb}} = \frac{2.7 \times 10^{-5}}{v_w} \left(\frac{\beta}{H_\star}\right) \left(\frac{T_n}{100\,\text{GeV}}\right) \left(\frac{g_*}{100}\right)^{1/6} \text{Hz}. \tag{B13}$$

APPENDIX C: THERMAL DEBYE MASS

The thermal Debye masses $\overline{m}_i$ are given by [45,48]

$$\overline{m}_i^2 = m_i^2 + \Pi_{ii}. \qquad (C1)$$

Within the context of the C2HDM, the self-energy corrections are written as follows [98]:

$$\Pi_{\Phi_1\Phi_1} = \begin{cases} \frac{1}{48}(12\lambda_1 + 8\lambda_3 + 4\lambda_4 + 3(3g^2 + g'^2))T^2, & \text{Type-I,} \\ \frac{1}{48}(12\lambda_1 + 8\lambda_3 + 4\lambda_4 + 3(3g^2 + g'^2) + 12y_b^2)T^2, & \text{Type-II,} \end{cases} \qquad (C2)$$

$$\Pi_{\Phi_2\Phi_2} = \begin{cases} \frac{1}{48}(12\lambda_2 + 8\lambda_3 + 4\lambda_4 + 3(3g^2 + g'^2) + 12y_t^2 + 12y_b^2)T^2, & \text{Type-I,} \\ \frac{1}{48}(12\lambda_2 + 8\lambda_3 + 4\lambda_4 + 3(3g^2 + g'^2) + 12y_t^2)T^2, & \text{Type-II,} \end{cases} \qquad (C3)$$

$$\Pi_{W^aW^a} = 2g^2T^2, \qquad (C4)$$

$$\Pi_{BB} = 2g'^2T^2. \qquad (C5)$$

[1] N. Aghanim *et al.* (Planck Collaboration), Planck 2018 results. VI. Cosmological parameters, Astron. Astrophys. **641**, A6 (2020).

[2] A. D. Sakharov, Violation of cp invariance, c asymmetry, and baryon asymmetry of the universe, Sov. Phys. Usp. **34**, 392 (1991).

[3] P. Huet and E. Sather, Electroweak baryogenesis and standard model *CP* violation, Phys. Rev. D **51**, 379 (1995).

[4] K. Kajantie, M. Laine, K. Rummukainen, and M. E. Shaposhnikov, Is there a hot electroweak phase transition at $m_H \gtrsim m_W$?, Phys. Rev. Lett. **77**, 2887 (1996).

[5] M. Trodden, Electroweak baryogenesis, Rev. Mod. Phys. **71**, 1463 (1999).

[6] A. G. Cohen, D. B. Kaplan, and A. E. Nelson, Progress in electroweak baryogenesis, Annu. Rev. Nucl. Part. Sci. **43**, 27 (1993).

[7] M. Carena, M. Quiros, and C. E. M. Wagner, Opening the window for electroweak baryogenesis, Phys. Lett. B **380**, 81 (1996).

[8] D. E. Morrissey and M. J. Ramsey-Musolf, Electroweak baryogenesis, New J. Phys. **14**, 125003 (2012).

[9] V. A. Kuzmin, V. A. Rubakov, and M. E. Shaposhnikov, On the anomalous electroweak baryon number nonconservation in the early Universe, Phys. Lett. **155B**, 36 (1985).

[10] P. Basler, M. Mühlleitner, and J. Wittbrodt, The *CP*-violating 2HDM in light of a strong first order electroweak phase transition and implications for Higgs pair production, J. High Energy Phys. 03 (2018) 061.

[11] P. Basler, M. Mühlleitner, and J. Müller, Electroweak phase transition in non-minimal Higgs sectors, J. High Energy Phys. 05 (2020) 016.

[12] G. Dorsch, S. Huber, K. Mimasu, and J. No, The Higgs vacuum uplifted: Revisiting the electroweak phase transition with a second Higgs doublet, J. High Energy Phys. 12 (2017) 086.

[13] H. Weicong, K. Zhaofeng, S. Jing, W. Peiwen, and Y. Jin, Min, New insights in the electroweak phase transition in the NMSSM, Phys. Rev. D **91**, 025006 (2015).

[14] C. Harman and S. Huber, Does zero temperature decide on the nature of the electroweak phase transition?, J. High Energy Phys. 06 (2016) 005.

[15] D. Gonçalves, A. Kaladharan, and Y. Wu, Electroweak phase transition in the 2HDM: Collider and gravitational wave complementarity, Phys. Rev. D **105**, 095041 (2022).

[16] T. Biekötter, S. Heinemeyer, J. M. No, M. O. Olea-Romacho, and G. Weiglein, The trap in the early Universe: impact on the interplay between gravitational waves and LHC physics in the 2HDM, J. Cosmol. Astropart. Phys. 03 (2023) 031.

[17] C. Grojean and G. Servant, Gravitational waves from phase transitions at the electroweak scale and beyond, Phys. Rev. D **75**, 043507 (2007).

[18] P. Athron, C. Balázs, A. Fowlie, L. Morris, and L. Wu, Cosmological phase transitions: From perturbative particle physics to gravitational waves, arXiv:2305.02357.

[19] C. Caprini *et al.*, Detecting gravitational waves from cosmological phase transitions with LISA: An update, J. Cosmol. Astropart. Phys. 03 (2020) 024.

[20] D. Bodeker, L. Fromme, S. J. Huber, and M. Seniuch, The Baryon asymmetry in the standard model with a low cut-off, J. High Energy Phys. 02 (2005) 026.

[21] L. Fromme and S. J. Huber, Top transport in electroweak baryogenesis, J. High Energy Phys. 03 (2007) 049.

[22] L. Fromme, S. J. Huber, and M. Seniuch, Baryogenesis in the two-Higgs doublet model, J. High Energy Phys. 11 (2006) 038.

[23] P. Basler, M. Mühlleitner, and J. Müller, BSMPT v2 a tool for the electroweak phase transition and the baryon asymmetry of the universe in extended Higgs Sectors, Comput. Phys. Commun. **269**, 108124 (2021).

[24] P. Basler, M. Mühlleitner, and J. Müller, Electroweak baryogenesis in the *CP*-violating two-Higgs doublet model, Eur. Phys. J. C **83**, 57 (2023).

[25] G. C. Branco, P. M. Ferreira, L. Lavoura, M. N. Rebelo, M. Sher, and J. P. Silva, Theory and phenomenology of two-Higgs-doublet models, Phys. Rep. **516**, 1 (2012).

[26] S. L. Glashow and S. Weinberg, Natural conservation laws for neutral currents, Phys. Rev. D **15**, 1958 (1977).

[27] E. A. Paschos, Diagonal neutral currents, Phys. Rev. D **15**, 1966 (1977).

[28] V. Andreev *et al.* (ACME Collaboration), Improved limit on the electric dipole moment of the electron, Nature (London) **562**, 355 (2018).

[29] D. Gonçalves, A. Kaladharan, and Y. Wu, Resonant top pair searches at the LHC: A window to the electroweak phase transition, Phys. Rev. D **107**, 075040 (2023).

[30] R. Coimbra, M. O. P. Sampaio, and R. Santos, ScannerS: Constraining the phase diagram of a complex scalar singlet at the LHC, Eur. Phys. J. C **73**, 2428 (2013).

[31] M. Mühlleitner, M. O. P. Sampaio, R. Santos, and J. Wittbrodt, ScannerS: Parameter scans in extended scalar sectors, Eur. Phys. J. C **82**, 198 (2022).

[32] B. W. Lee, C. Quigg, and H. B. Thacker, Weak interactions at very high-energies: The role of the Higgs boson mass, Phys. Rev. D **16**, 1519 (1977).

[33] S. Kanemura, T. Kubota, and E. Takasugi, Lee-Quigg-Thacker bounds for Higgs boson masses in a two doublet model, Phys. Lett. B **313**, 155 (1993).

[34] I. F. Ginzburg and I. P. Ivanov, Tree-level unitarity constraints in the most general 2HDM, Phys. Rev. D **72**, 115010 (2005).

[35] I. P. Ivanov, M. Köpke, and M. Mühlleitner, Algorithmic boundedness-from-below conditions for generic scalar potentials, Eur. Phys. J. C **78**, 413 (2018).

[36] W. G. Hollik, G. Weiglein, and J. Wittbrodt, Impact of vacuum stability constraints on the phenomenology of supersymmetric models, J. High Energy Phys. 03 (2019) 109.

[37] P. M. Ferreira, M. Mühlleitner, R. Santos, G. Weiglein, and J. Wittbrodt, Vacuum instabilities in the N2HDM, J. High Energy Phys. 09 (2019) 006.

[38] P. Bechtle, D. Dercks, S. Heinemeyer, T. Klingl, T. Stefaniak, G. Weiglein, and J. Wittbrodt, HiggsBounds-5: Testing Higgs sectors in the LHC 13 TeV era, Eur. Phys. J. C **80**, 1211 (2020).

[39] P. Bechtle, S. Heinemeyer, T. Klingl, T. Stefaniak, G. Weiglein, and J. Wittbrodt, HiggsSignals-2: Probing new

physics with precision Higgs measurements in the LHC 13 TeV era, Eur. Phys. J. C **81,** 145 (2021).

[40] O. Atkinson, M. Black, C. Englert, A. Lenz, A. Rusov, and J. Wynne, The flavourful present and future of 2HDMs at the collider energy frontier, J. High Energy Phys. 11 (2022) 139.

[41] S. Coleman and E. Weinberg, Radiative corrections as the origin of spontaneous symmetry breaking, Phys. Rev. D **7,** 1888 (1973).

[42] C.-W. Chiang, M. J. Ramsey-Musolf, and E. Senaha, Standard model with a complex scalar singlet: Cosmological implications and theoretical considerations, Phys. Rev. D **97,** 015005 (2018).

[43] O. Gould and T. V. I. Tenkanen, On the perturbative expansion at high temperature and implications for cosmological phase transitions, J. High Energy Phys. 06 (2021) 069.

[44] J. E. Camargo-Molina, A. P. Morais, R. Pasechnik, M. O. P. Sampaio, and J. Wessén, All one-loop scalar vertices in the effective potential approach, J. High Energy Phys. 08 (2016) 073.

[45] P. Basler, M. Krause, M. Muhlleitner, J. Wittbrodt, and A. Wlotzka, Strong first order electroweak phase transition in the *CP*-conserving 2HDM revisited, J. High Energy Phys. 02 (2017) 121.

[46] J. Elias-Miro, J. R. Espinosa, and T. Konstandin, Taming infrared divergences in the effective potential, J. High Energy Phys. 08 (2014) 034.

[47] S. P. Martin, Taming the Goldstone contributions to the effective potential, Phys. Rev. D **90,** 016013 (2014).

[48] P. B. Arnold and O. Espinosa, The effective potential and first order phase transitions: Beyond leading-order, Phys. Rev. D **47,** 3546 (1993).

[49] T. Matsubara, A new approach to quantum statistical mechanics, Prog. Theor. Phys. **14,** 351 (1955).

[50] M. Quiros, Finite temperature field theory and phase transitions, in *ICTP Summer School in High-Energy Physics and Cosmology* (World Scientific, Singapore, 1999), Vol. 1, pp. 187–259.

[51] H. H. Patel and M. J. Ramsey-Musolf, Baryon washout, electroweak phase transition, and perturbation theory, J. High Energy Phys. 07 (2011) 029.

[52] C. Wainwright, S. Profumo, and M. J. Ramsey-Musolf, Gravity waves from a cosmological phase transition: Gauge artifacts and Daisy resummations, Phys. Rev. D **84,** 023521 (2011).

[53] D. Metaxas and E. J. Weinberg, Gauge independence of the bubble nucleation rate in theories with radiative symmetry breaking, Phys. Rev. D **53,** 836 (1996).

[54] M. Garny and T. Konstandin, On the gauge dependence of vacuum transitions at finite temperature, J. High Energy Phys. 07 (2012) 189.

[55] S. Arunasalam and M. J. Ramsey-Musolf, Tunneling potentials for the tunneling action: Gauge invariance, J. High Energy Phys. 08 (2022) 138.

[56] J. Hirvonen, J. Löfgren, M. J. Ramsey-Musolf, P. Schicho, and T. V. I. Tenkanen, Computing the gauge-invariant bubble nucleation rate in finite temperature effective field theory, J. High Energy Phys. 07 (2022) 135.

[57] J. Löfgren, M. J. Ramsey-Musolf, P. Schicho, and T. V. I. Tenkanen, Nucleation at finite temperature: A gauge-invariant perturbative framework, Phys. Rev. Lett. **130,** 251801 (2023).

[58] N. K. Nielsen, On the gauge dependence of spontaneous symmetry breaking in gauge theories, Nucl. Phys. **B101,** 173 (1975).

[59] P. Athron, C. Balazs, A. Fowlie, L. Morris, G. White, and Y. Zhang, How arbitrary are perturbative calculations of the electroweak phase transition?, J. High Energy Phys. 01 (2023) 050.

[60] A. D. Linde, Fate of the false vacuum at finite temperature: Theory and applications, Phys. Lett. **100B,** 37 (1981).

[61] S. R. Coleman, The fate of the false vacuum. 1. Semiclassical Theory, Phys. Rev. D **15,** 2929 (1977).

[62] C. L. Wainwright, CosmoTransitions: Computing cosmological phase transition temperatures and bubble profiles with multiple fields, Comput. Phys. Commun. **183,** 2006 (2012).

[63] J. M. Moreno, M. Quiros, and M. Seco, Bubbles in the supersymmetric standard model, Nucl. Phys. **B526,** 489 (1998).

[64] C. Caprini *et al.*, Science with the space-based interferometer eLISA. II: Gravitational waves from cosmological phase transitions, J. Cosmol. Astropart. Phys. 04 (2016) 001.

[65] A. Alves, D. Gonçalves, T. Ghosh, H.-K. Guo, and K. Sinha, Di-Higgs production in the 4*b* channel and gravitational wave complementarity, J. High Energy Phys. 03 (2020) 053.

[66] A. Alves, D. Gonçalves, T. Ghosh, H.-K. Guo, and K. Sinha, Di-Higgs blind spots in gravitational wave signals, Phys. Lett. B **818,** 136377 (2021).

[67] P. Amaro-Seoane *et al.* (LISA Collaboration), Laser Interferometer Space Antenna, arXiv:1702.00786.

[68] P. Athron, C. Balázs, and L. Morris, Supercool subtleties of cosmological phase transitions, J. Cosmol. Astropart. Phys. 03 (2023) 006.

[69] C. Badger *et al.*, Probing early Universe supercooled phase transitions with gravitational wave data, Phys. Rev. D **107,** 023511 (2023).

[70] W. Grimus, L. Lavoura, O. M. Ogreid, and P. Osland, A precision constraint on multi-Higgs-doublet models, J. Phys. G **35,** 075001 (2008).

[71] J. M. Gerard and M. Herquet, A twisted custodial symmetry in the two-Higgs-doublet model, Phys. Rev. Lett. **98,** 251802 (2007).

[72] J. M. Cline and K. Kainulainen, Electroweak baryogenesis at high bubble wall velocities, Phys. Rev. D **101,** 063525 (2020).

[73] K. Kainulainen, T. Prokopec, M. G. Schmidt, and S. Weinstock, First principle derivation of semiclassical force for electroweak baryogenesis, J. High Energy Phys. 06 (2001) 031.

[74] K. Kainulainen, T. Prokopec, M. G. Schmidt, and S. Weinstock, Semiclassical force for electroweak baryogenesis: Three-dimensional derivation, Phys. Rev. D **66,** 043502 (2002).

[75] T. Prokopec, M. G. Schmidt, and S. Weinstock, Transport equations for chiral fermions to order h-bar and electroweak baryogenesis. Part II, Ann. Phys. (Amsterdam) **314,** 267 (2004).

[76] T. Prokopec, M. G. Schmidt, and S. Weinstock, Transport equations for chiral fermions to order h bar and electroweak

baryogenesis. Part 1, Ann. Phys. (Amsterdam) **314,** 208 (2004).

[77] J. M. Cline, M. Joyce, and K. Kainulainen, Supersymmetric electroweak baryogenesis, J. High Energy Phys. 07 (2000) 018.

[78] P. Huet and A. E. Nelson, Electroweak baryogenesis in supersymmetric models, Phys. Rev. D **53,** 4578 (1996).

[79] G. D. Moore, Computing the strong sphaleron rate, Phys. Lett. B **412,** 359 (1997).

[80] G. D. Moore, Sphaleron rate in the symmetric electroweak phase, Phys. Rev. D **62,** 085011 (2000).

[81] A. Riotto, Towards a nonequilibrium quantum field theory approach to electroweak baryogenesis, Phys. Rev. D **53,** 5834 (1996).

[82] M. Postma, J. van de Vis, and G. White, Resummation and cancellation of the VIA source in electroweak baryogenesis, J. High Energy Phys. 12 (2022) 121.

[83] R.-G. Cai, Z. Cao, Z.-K. Guo, S.-J. Wang, and T. Yang, The gravitational-wave physics, Natl. Sci. Rev. **4,** 687 (2017).

[84] C. Caprini and D. G. Figueroa, Cosmological backgrounds of gravitational waves, Classical Quantum Gravity **35,** 163001 (2018).

[85] A. Kosowsky, M. S. Turner, and R. Watkins, Gravitational radiation from colliding vacuum bubbles, Phys. Rev. D **45,** 4514 (1992).

[86] A. Kosowsky and M. S. Turner, Gravitational radiation from colliding vacuum bubbles: Envelope approximation to many bubble collisions, Phys. Rev. D **47,** 4372 (1993).

[87] R. Jinno and M. Takimoto, Gravitational waves from bubble collisions: An analytic derivation, Phys. Rev. D **95,** 024009 (2017).

[88] M. Kamionkowski, A. Kosowsky, and M. S. Turner, Gravitational radiation from first order phase transitions, Phys. Rev. D **49,** 2837 (1994).

[89] S. J. Huber and T. Konstandin, Gravitational wave production by collisions: More bubbles, J. Cosmol. Astropart. Phys. 09 (2008) 022.

[90] M. Hindmarsh, S. J. Huber, K. Rummukainen, and D. J. Weir, Shape of the acoustic gravitational wave power spectrum from a first order phase transition, Phys. Rev. D **96,** 103520 (2017).

[91] M. Hindmarsh, S. J. Huber, K. Rummukainen, and D. J. Weir, Gravitational waves from the sound of a first order phase transition, Phys. Rev. Lett. **112,** 041301 (2014).

[92] M. Hindmarsh, Sound shell model for acoustic gravitational wave production at a first-order phase transition in the early Universe, Phys. Rev. Lett. **120,** 071301 (2018).

[93] H.-K. Guo, K. Sinha, D. Vagie, and G. White, Phase transitions in an expanding Universe: Stochastic gravitational waves in standard and non-standard histories, J. Cosmol. Astropart. Phys. 01 (2021) 001.

[94] M. B. Hindmarsh, M. Lüben, J. Lumma, and M. Pauly, Phase transitions in the early Universe, SciPost Phys. Lect. Notes **24,** 1 (2021).

[95] D. Bodeker and G. D. Moore, Electroweak bubble wall speed limit, J. Cosmol. Astropart. Phys. 05 (2017) 025.

[96] E. Witten, Cosmic separation of phases, Phys. Rev. D **30,** 272 (1984).

[97] C. Caprini, R. Durrer, and G. Servant, The stochastic gravitational wave background from turbulence and magnetic fields generated by a first-order phase transition, J. Cosmol. Astropart. Phys. 12 (2009) 024.

[98] D. Comelli and J. R. Espinosa, Bosonic thermal masses in supersymmetry, Phys. Rev. D **55,** 6253 (1997).